Electrochemical Measurement of Intrinsic Oxygen Reduction Reaction Activity at High Current Densities as a Function of Particle Size for $Pt_{4-x}Co_x$ /C (x=0,1,3) Catalysts

Christopher Zalitis[B], Anthony Kucernak[A,*†], Xiaoqian Lin[A], Jonathan Sharman[B]

[A]Department of Chemistry, Imperial College London, London SW7 2AZ, United Kingdom
[B]Johnson Matthey Technical Centre, Blount's Court, Sonning Common, Reading RG4 9NH, UK

Abstract

While extensive literature shows Pt alloy catalysts are a more active substitute for pure Pt catalysts at 0.9 V, high activity is also needed at high current densities if they are to be adopted for fuel cell application. We use a newly developed electrochemical technique to compare the performance of a range of catalysts with initial composition $Pt_{4-x}Co_x$/C of different particle sizes at high current densities (~0.65 V) as well as the typical ~0.9 V . Moving from 0.9 V to 0.65 V the current densities were found to increase by up to 80-fold for the Pt/C catalysts, with this factor decreasing as the amount of Co in the PtCo alloy increases. A kinetic model incorporating site blocking species at both high and low potentials has been used to explain this change. While the de-alloyed catalysts were found to have a greater mass activity at low current densities (~0.9 V) they were no longer as active as 2.1 nm Pt particle catalyst at high current densities (~0.65 V). However, for equivalent particle sizes, the mass activity of the dealloyed Co-containing catalysts remains higher across the normal operating potentials of a fuel cell. Using this insight, we predict that at 0.65 V a catalyst composed of 3.8 nm $CoPt@Pt_{1ML}$ particles would give optimum mass activity performance. In addition, two peaks were observed during the CV of the ORR on pure Pt nanoparticles in the hydrogen adsorption region (0 – 0.4 V). These peaks are associated with surface sites with different reactivity towards the ORR.

Keywords: Oxygen reduction reaction, fuel cells, electrocatalysis, platinum, cobalt

TOC Graphic:

---
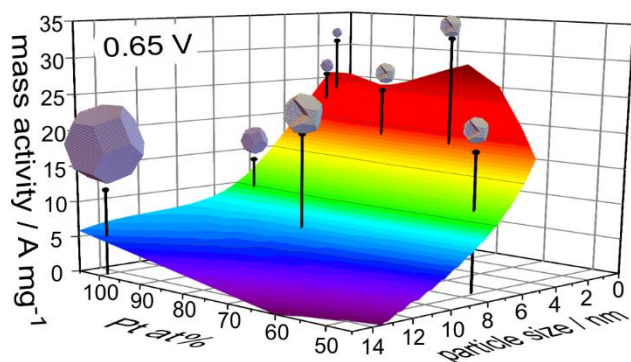
* corresponding author: anthony@imperial.ac.uk, Ph: +44 2075945831, Fax:+44 2075945804

1   Introduction

For the commercialization of polymer electrolyte fuel cell (PEFC) technology, the DOE have set out a comprehensive roadmap [1]. One of the most difficult challenges has been to improve the oxygen reduction catalyst at the cathode side, with a mass activity target of 0.44 A mg$^{-1}_{Pt}$ at 0.9 V vs. RHE[1]. State of the art Pt/C catalysts have a mass activity of ~0.26 A mg$^{-1}_{Pt}$ in membrane electrode assembly (MEA) testing [2], somewhat short of the DOE target. This has led to a thorough investigation of alloying and shape control of platinum containing catalysts, with many combinations vastly exceeding the DOE target in ex-situ testing. Such examples include PtNi/C nanoparticles [3-4], Pt$_3$Ni/C nanoframes [5-6], Mo-Pt$_3$Ni/C nanoparticles [7], PtPb-Pt nanoplates [8] and jagged Pt nanowires [9], with activity gains of up to 30× the DOE target. In a similar vein, Toyota have recently commercialized the Mirai with a Pt$_9$Co$_1$/C alloy catalyst [10].

However for those catalysts which have been tested in both the RDE and MEA configurations [4, 6], the activity values are lower by at least a factor of 2 in the MEA which shows that achieving RDE activities in a MEA is not straight forward. Even with this reduced performance, some of these catalysts still exceed the DOE target with Han *et al.* [4] showing BOL and even EOL mass activities of 0.65 and 0.51 A mg$^{-1}_{Pt}$, respectively. However, shaped nanoparticles have suffered larger activity reductions in the MEA environment highlighting the different conditions the catalyst is exposed to and the problems reproducing results from the RDE in an MEA[6, 11]. These studies again highlight that more than just the RDE should be used on the road to catalyst development and commercialization. Meeting the low current density (0.9 V vs. RHE) mass activity target has been a significant achievement of recent times and has shifted the focus for catalyst development to performance at high current density (0.6 – 0.8 V vs. RHE) [12], where PEFCs are expected to generated the majority of energy.

Understanding of catalyst performance at high current densities is still limited as there are few techniques capable of achieving the high current densities of a fuel cell while still measuring the intrinsic catalyst performance. Applicable approaches include the solid state TEM grid electrode [13] and the floating electrode [14] developed within this group, the much higher loaded GDE from Pinaud *et al.* [15], and the introduction of membrane onto a GDE from Inaba *et al.*[16] [17]. Low loading MEAs are also beginning to be published with a greater focus on intrinsic performance [18-19].

Within this paper we use the floating electrode to assess the performance of Pt/C and de-alloyed PtCo/C catalysts at different particle sizes. The measurements are optimized for studying catalytic activity at the high current densities expected in an operating fuel cell and we show how we can model the electrokinetic performance of these catalysts. In addition, this paper looks at some of the intrinsic features of Pt across a wide potential window of the ORR (-0.02 – 1 V vs RHE), revealing two peaks in the hydrogen adsorption region (< 0.4 V vs. RHE) similar to those observed in the hydrogen oxidation reaction (HOR) [20].

2   Experimental

Catalysts in the series Pt$_{4-x}$Co$_x$ /C (x=0,1,3) were examined in this study. For x = 0, this corresponds to Pt/C catalysts and for x=(1,3) this corresponds to two different PtCo/C catalysts each at two different particle sizes. Note that the numbers correspond to initial composition and after the dealloying process the Pt:Co ratio is increased. Our terminology is that d-Pt$_x$Co$_y$ means a material that was dealloyed and which had an

initial Pt:Co ratio of x:y, before dealloying. d-PtCo/C at two different initial Pt:Co ratios were supplied by Johnson Matthey. The Pt/C catalysts of different particle size are the same as those in ref [20], where more details can be found. A brief summary of their properties is presented in Table 1. The d-PtCo/C catalysts were fabricated through base hydrolysis at low (Pt_3Co) and high ($PtCo_3$) cobalt alloy ratios. Each of these sets were then annealed under reducing conditions to give two particle sizes for each alloy ratio. The alloy catalysts were acid leached in H_2SO_4 forming particles with reduced Co content in the core and a Pt skin on the surface. The data in Table 1 corresponds to the properties after the leaching process.

Table 1. Catalyst properties | Particle size (determined from TEM and XRD), CO-chemisorption surface area, and metal loading and composition of catalysts used in this study. For PtCo/C materials, properties were measured after dealloying.

Catalyst type	Particle size / nm		CO metal area[b] / $m^2\,g^{-1}$	Metal loading[c] / wt%		Alloy fraction / at%	
	XRD[a]	TEM		Pt	Co	Pt	Co
Pt/C[d]	13.3	14.6 ± 6.6	13	41.4		100	
Pt/C[d]	6.2	6.9 ± 2.3	28	40.0		100	
Pt/C[d]	3.6[e]	2.7 ± 1.2	77	42.8		100	
Pt/C[d]	< 2	2.1 ± 0.5	121	38.2		100	
d-Pt₃Co/C	3.8	4.6 ± 2.2	35	36.8	2.8	79.7	20.3
d-Pt₃Co/C	5.4	9.4 ± 3.4	25	36.9	3.1	78.1	21.9
d-PtCo₃/C	‡	5.1 ± 2.4	32	26.0	4.5	63.5	36.5
d-PtCo₃/C	‡	7.2 ± 3.2	27	24.6	7.2	50.9	49.1

a. Based on 5 reflections
b. CO chemisorption
c. ICP-ES measurement
d. Analysis from previous paper [20]
e. Bimodal distribution
‡ Shows poor crystallinity

Floating electrodes were prepared by the standard method [14]. A 100 nm gold layer was sputter deposited (Emitech K575X) onto an ultra-flat porous polycarbonate track-etched (PCTE) filtration membrane (400 nm pore size, 47 mm diameter, PCT0447100, Sterlitech) to form a conductive substrate. This was then cleaned by Soxhlet washing in propan-2-ol and then water for 8 hours each. A catalyst ink containing one of the catalysts in Table 1 was then deposited by vacuum filtration onto the surface to form a 2 mm diameter spot. Pre-concentrated catalyst ink was made containing a mixture of catalyst (50 mg), butyl acetate (Sigma, anhydrous grade, 950 mg), propan-2-ol (VWR, Normapur analytical reagent, 570 mg) and perfluorosulfonic acid (PFSA) solution (DuPont DE521 Nafion™ solution, 5 wt. %, 380 mg). For deposition, the volume of ink required to reach the target loading was further diluted to 500 µl with a mixture of 50:50 butyl acetate:propan-2-ol. This solution was then filtered under vacuum onto the gold coated PCTE membrane. Finally, the back of the electrode was hydrophobized with a coating of amorphous fluoropolymer (DuPont DeNemour, Teflon™ AF 2400) dissolved in Fluorinert FC-40 (Sigma, F9755) to achieve a loading of $0.21\ \mu g\ cm^{-2}_{Geo}$. Enough catalyst was deposited to achieve an electrode with catalyst roughness factor (ratio of catalyst specific area to electrode geometric area) of between 1-2. This required a catalyst loading of $2 - 25\ \mu g_{Pt}\ cm^{-2}_{geo}$ depending on the actual catalyst (lowest loading for 2.1 nm Pt/C, highest loading for 13 nm Pt/C).

High purity perchloric acid (VWR, Merck Suprapur®, 4 mol dm^{-3}) and gases (≥ 5.8 N, Air Products, BIP plus) were used. All glassware was put through a cleaning procedure consisting of soaking in acidified potassium permanganate (0.025 mol dm^{-3} KMnO$_4$, 0.2 mol dm^{-3} H$_2$SO$_4$) for 8 h, rinsed with acidified hydrogen peroxide (0.2 mol dm^{-3} H$_2$O$_2$, 0.3 mol dm^{-3} H$_2$SO$_4$) and then boiled in ultra-pure water, while being rinsed at least 6 times with ultra-pure water between each step and before use. A water jacketed three electrode electrochemical cell was kept at 298 K for all measurements. The Pt wire counter electrode was in a glass frit compartment and the cell used an in house produced reversible hydrogen electrode (RHE) in a Luggin capillary compartment.

A Gamry 600 potentiostat was used for electrochemical measurements. All electrodes were cleaned by alternating ten-times between the oxygen reduction reaction (ORR, O$_2$ in gas space), and hydrogen oxidation reaction (HOR, H$_2$ in gas space), purging the gas space above the electrode with nitrogen between the consecutive tests. The ORR scans involved two cyclic voltammograms (CVs) from 1.0V – 0.0 V vs. RHE at 50 mV s^{-1}, and the HOR scans involved two CVs between -0.1 – 1.0 V vs. RHE at 50 mV s^{-1}. The HOR (-0.1 – 1 V vs. RHE at 10 mV s^{-1}) and ORR (1 – 0.3 or -0.02 V vs. RHE at 10 mV s^{-1}) CVs were taken immediately after cleaning. After the measurements the solution and gas headspace were purged with nitrogen and a CV collected at the same scan rate and potential window as the ORR. These voltammograms were used to perform a double layer capacitance correction. A further CV (0.075 – 1 V vs. RHE at 20 mV s^{-1}) was used to estimate the catalyst surface area through integration of the H$_{upd}$ region after double layer capacitance correction. With our current experimental configuration, it is difficult to perform CO$_{ads}$ stripping experiments directly on the floating electrodes, hence instead we use H$_{upd}$ experiments to measure the surface area. For comparison, the surface area of each of the PtCo/C catalysts were measured using H$_{upd}$ and CO$_{ads}$ stripping using films deposited on a glassy carbon disk (see supporting information section, figures s7-s9). We find that ECSAs for these catalysts show a direct correlation between H$_{UPD}$ and CO$_{ads}$ stripping measurements with the CO$_{ads}$ stripping measurement matching the CO Chemisorption surface areas. While single crystal studies have shown the charge associated with the H$_{upd}$ decreases with respect to polycrystalline Pt value of 210 μC cm^{-2} with increasing Co or Ni content in Pt metal alloys [21-23], we nonetheless see a constant difference of 1.28-times more surface area when using CO$_{ads}$ stripping compared to H$_{upd}$ measurements. In this paper we use the H$_{UPD}$ calculated surface areas to calculate the specific activity, although the value above can be used to convert our specific activities to those associated with CO$_{ads}$ stripping. Uncompensated resistance was measured using the high frequency intercept of an impedance scan for each electrode (measured at 0.4 V vs. RHE, 100 kHz – 1 Hz, 10 mV amplitude). In this way, all ORR curves are iR and double layer (DL) corrected. For each catalyst, three electrodes were run with an average for each catalyst given and a graph presenting the curve most representative of the average shown for clarity; an example of three runs is shown in the supporting information Figure s10.

2.1 Characterization

Particle sizes were measured using powder X-ray diffraction (XRD) and high-resolution transmission electron microscopy (HRTEM), Figure 1. X-ray diffraction data were collected using Cu Kα radiation (λ = 1.5406 and 1.54439 Å) on a Bruker AXS D8. Crystallite sizes have been calculated from the Rietveld refinements using the LVol-IB method. In Figure 1, the Pt$_3$Co indices are shown for the d-Pt$_3$Co/C catalysts

and the PtCo indices are shown for the d-PtCo$_3$/C catalysts, while Figure s2 shows a comparison between the PtCo$_3$ and PtCo indices against the d-PtCo$_3$/C catalysts.

Metal surface areas were determined through pulsed CO chemisorption in a helium carrier gas using a Micromeritics Autochem II chemisorption analyzer.

A JEOL JEM 2800 (Scanning) transition electron microscope at 200 kV with a C2 aperture of 70 and 40 μm was used to image Pt nanoparticle diameters using bright field imaging for at least 100 nanoparticles with the number average presented for each sample. Catalysts are represented using their TEM size as it gives a particle number size distribution and because the high Co content nanoparticle were not crystalline enough to measure particle size by XRD.
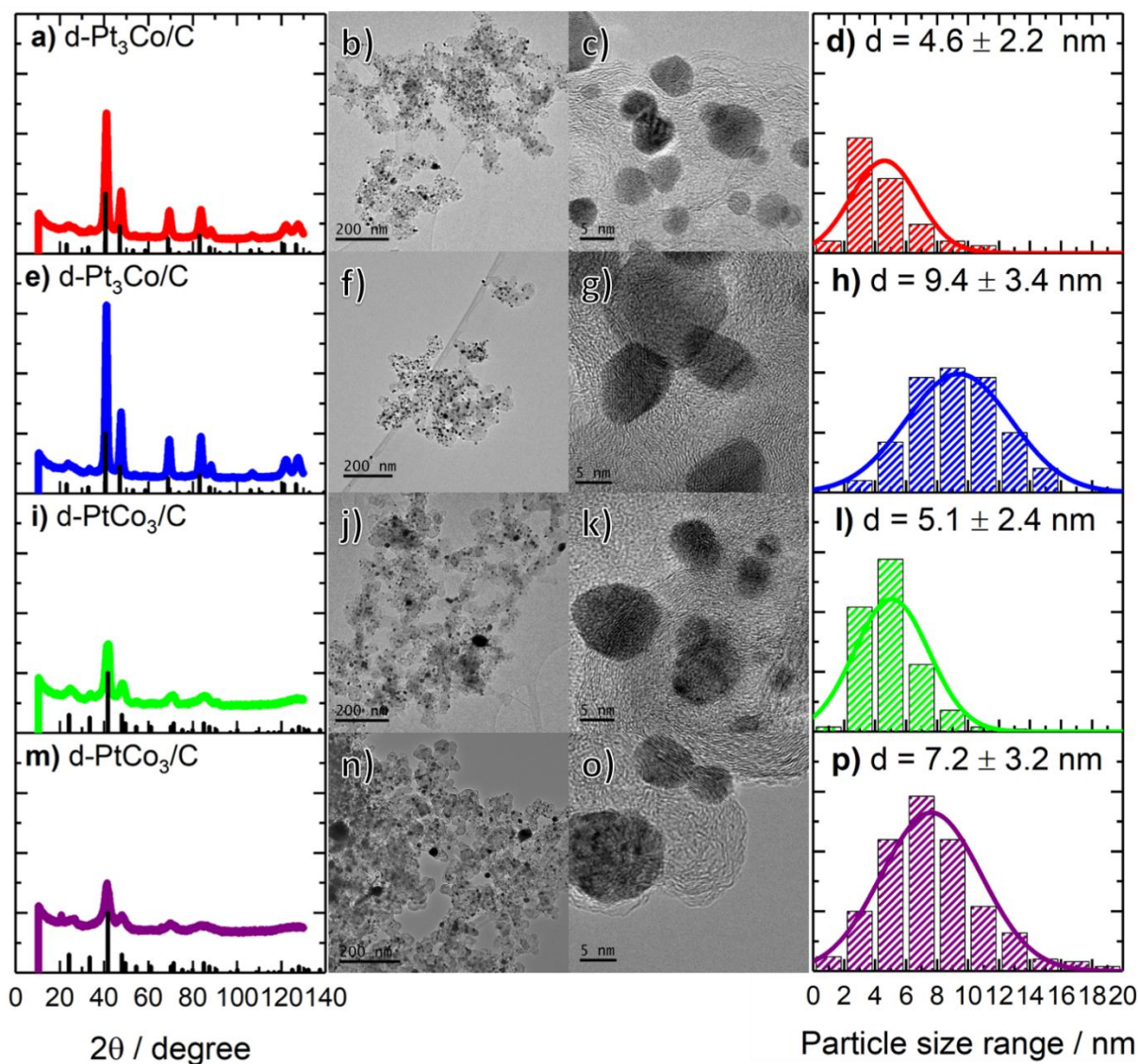

Figure 1. Ex-situ characterization of the d-PtCo/C catalysts using XRD and TEM | for each catalyst d-Pt$_3$Co/C and d-PtCo$_3$/C, the XRD pattern (a), e), i), m)), low resolution TEM with a 200 nm scale bar (b), f), j), n)), high resolution TEM with 5 nm scale bar (c),

3 Results and discussion

In the results presented below we first consider the effect of the dealloying process on forming Pt skin alloy nanoparticles and then consider the performance of a range of catalysts of initial composition $Pt_{4-x}Co_x$ /C (x=0,1,3) as a function of particle size. The analysis considers the performance at high potential initially, and then the performance at progressively lower potentials, and how the exposure of the catalyst to low potentials affects its performance.

3.1 Dealloying process

As previously discussed, the initial Pt_3Co and $PtCo_3$ alloy catalysts underwent a dealloying process to produce particles with a Pt rich skin covering the PtCo alloy core. During the dealloying process cobalt dissolves from the particle to leave a platinum rich skin of between 2 – 3 nm thick (observed at ~0.8 nm thick, see supporting information) and shifts the composition of the particle to a higher platinum content. For small particles and high cobalt content it might not be possible to stabilize cobalt in the particles during the dealloying process resulting in all the cobalt being removed during dealloying. For larger particles the size of the unstable composition region decreases as it is more likely that a Pt skin can form over the Co rich core which then prevents further Co dissolution. Experimentally, it is observed that larger particles with more Co are more likely to form porous structures. This is exemplified in Figure 1(o) where the two particles towards the top right which represent the majority of the particles in size distribution do not have porosity, while the large particle center left shows porosity; as this is on the tail of the particle size distribution there is not a significant number of them and therefore are not expected to contribute significantly to the activity. High resolution TEM (Figure 1) and line scans (section 5, supporting information) do not suggest that there is any significant internal porosity for these particles, although the higher Co content particles have a somewhat more heterogeneous structure. In Figure 2(a) we provide results on calculations associated with the dealloying process (for the calculation procedure, please see the supporting information).
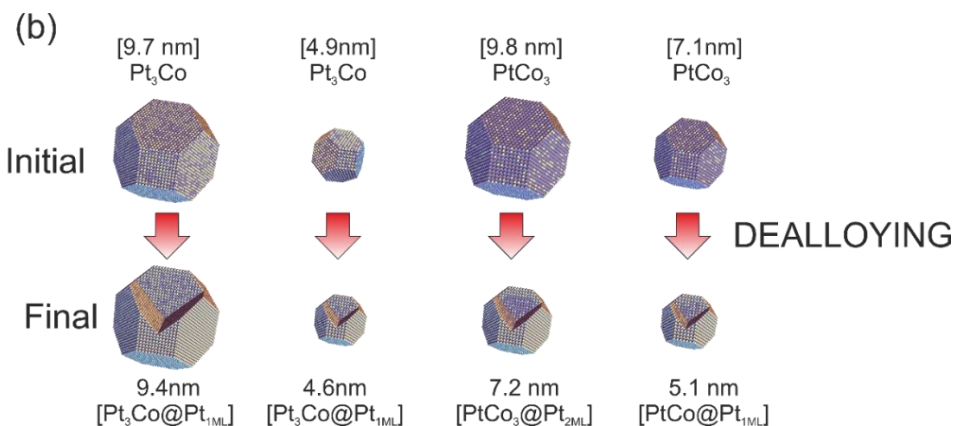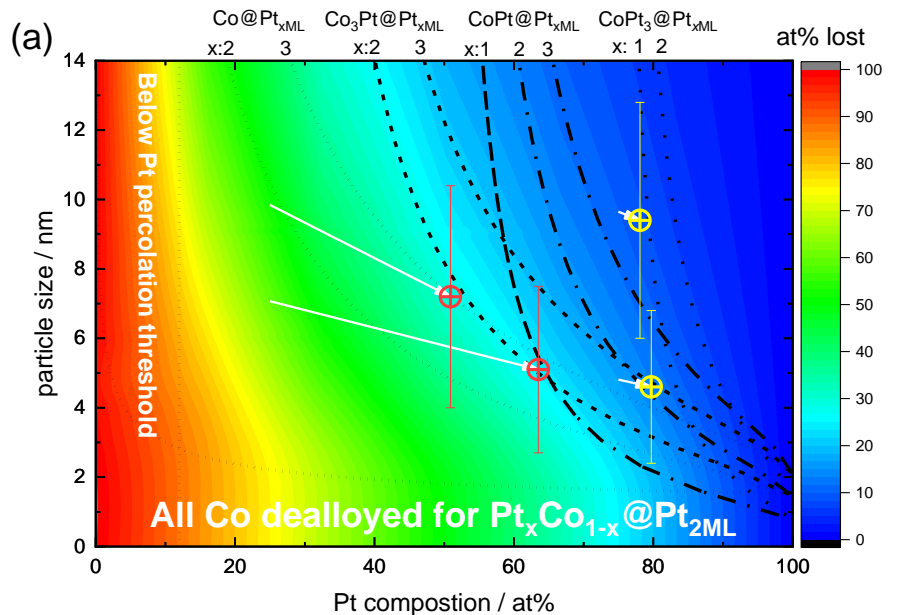
Figure 2. Dealloying processes to produce Pt$_x$Co$_{1-x}$@Pt$_{YML}$ particles. | (a) Compositional variation diagram for understanding the processes involved during dealloying of PtCo alloys. Colors represent the at% dissolution which occurs in order to produce a truncated octahedron particle with a core of the initial composition and coated with two monolayers of platinum. The Co@Pt$_{xML}$(x=2,3), PtCo$_3$@Pt$_{xML}$(x=2,3), and Pt$_3$Co@Pt$_{xML}$(x=1,2) lines represent particle diameter versus net composition for those specific types of particles. The dotted line at particle diameter = 2 nm (high Pt content) curving up at low Pt content represents the minimum particle size below which all Co in the particle is dealloyed. The vertical line at 12at% Pt represents the platinum percolation threshold, to the left of this line, particles will almost certainly disintegrate when all the Co is removed. The four d-PtCo/C catalysts are drawn as circles with their respective predicted dealloying profile (white arrows from initial to final composition) (b) Cartoons illustrating the dealloying processes which have occurred for our particles for both Co rich (PtCo$_3$) and Co poor (Pt$_3$Co) alloys. The initial particle sizes are calculated from the final particle sizes assuming all the Pt in the particle is conserved. The structures of the final particles are estimated from the particle sizes, final composition and initial composition of the particles. Octants of the particle are removed so that Pt skin formation can be seen. Error bars in (a) represent the standard deviation in particle sizes from Table 1.

The diagram plots particle size versus composition and covers the compositional space between pure Co to pure Pt and particle diameters from zero to 14 nm. The calculations assume that the end result of dealloying is a particle with a Co-rich core of defined composition having a truncated octahedral geometry (see supporting information) covered by two monolayers of pure Pt (except for the specific dashed lines, which represent the extra cases of three or one overlayer of Pt). The platinum for the monolayers

surrounding the core are produced through the complete removal of Co from outer layers [26-27]. We note that these cases represent ideal situations in which the formation of a Pt shell stabilizes the alloy core, and the calculations assume a homogeneous composition of the initial particle and for the final particle a core of homogeneous composition surrounded by a pure platinum shell. Under certain conditions or treatments, differences in the manner in which the dealloying process occurs may lead to more severe dealloying of the particles, leading to porous particles, shell-like particles, or pure Pt particles[28]. Hence in these calculations we have examined two separate cases. In the first case, the core retains the same composition as the initial particle. On the basis of XRD results, this appears to be the case with Pt rich initial compositions where the d-Pt_3Co/C catalysts appear to maintain a Pt_3Co core composition. The other case is where the core also undergoes some dealloying. This appears to be the case for the catalysts with an initial $PtCo_3$ composition, in which XRD results suggest that a Pt_1Co_1 core is produced, Figure s2. This is in line with previous observations for $PtNi_3$ and $PtNi_5$ nanoparticles dealloyed through electrochemical cycling [29-30]. In order to demarcate these different aspects, we add extra lines on Figure 2(a) representing the composition CoPt@Pt_{xML}.

The red and yellow points in Figure 2(a) represent the final composition and average size (error bars represent standard deviations) of the d-PtCo catalysts we have used. The lower dotted line represents the limit below which all Co will be dealloyed in forming the two Pt overlayers - i.e. any initial particle within this compositional region will end up as a pure Pt particle upon dealloying. The vertical dotted line at 12 at% Pt represents the percolation threshold[31]. Simply put, to the left of this line, the Pt atoms in the initial particle are not attached to each other and thus during the dealloying process, the particle will likely entirely dissolve and disintegrate.

The nine other dotted curves represent the limiting composition/particle size curves for particles with cores of Co, $PtCo_3$, PtCo and Pt_3Co coated with a specific number of layers Pt (3: Pt_{3ML}, 2: Pt_{2ML}, 1: Pt_{1ML}) – these represent ideal structures. The Co@Pt_{2ML} represents the limit of composition of core-shell particles which are composed of a 2ML Pt overlayer – any composition to the left and below is not physically possible (i.e. although it is possible to have a **homogeneous** particle with that composition, it is not possible to have a core-shell particle with a 2ML platinum skin with that composition). A consequence of this is that any **initial** composition in the area below and to the left of that line is unstable with respect to Co dissolution and hence during the dealloying process, the particle composition and size will shift across that line (see supporting information for more details of the dealloying process).

The color gradations represent the %atoms lost from the initial particle during the dealloying process (as Co). The measured total composition of the dealloyed catalysts used in this work are indicated on the graph - the red points represent the Co rich particles. The smaller of these sits close to both the Co_3Pt@Pt_{2ML} and CoPt@Pt_{1ML} lines. On the basis of XRD results suggesting a PtCo core (see SI Figure s2), we interpret the composition as being close to CoPt@Pt_{1ML}. The larger particle sits close to the Co_3Pt@Pt_{2ML} and Co@Pt_{3ML} lines. We would not expect the core to become more Co rich than the starting particle, hence this suggests that the composition is moderately well described by two layers of Pt on top of a Co_3Pt core. This is in agreement with an estimated 2-3 Pt layers from the lines scan of the d-$PtCo_3$/C catalyst at 7.2 nm particle size (see supporting information, Figure s3b). The other two catalysts (yellow) represent the dealloyed particles which are more Pt rich with their compositions and particle sizes close

to the $Pt_3Co@Pt_{1ML}$ line. This suggests that the Pt rich phases do not require as thick a Pt overlayer to stabilize the composition as the Co rich cores do. The Pt skin for the line scans of the d-Pt_3Co/C catalyst at 9.4 nm particle size is hardly discernable, with a possibly only a monolayer (see Figure s3b Supporting information). This aspect makes sense from a corrosion viewpoint, as dissolution of Co will be hindered in high Pt content alloys. The white arrows in Figure 2(a) represent the compositional change which occurs during the dealloying process to produce the morphologies described (NB in the supporting information we also provide examples of dealloying "trajectories" i.e. initial and final particle size/compositions under the assumption of the initial and compositions shown in Figure 2(b)). Figure 2(b) provides cartoons of the dealloying process (i.e. beginning and end of each of the arrows), showing the initial size of the catalyst particles (calculated assuming no platinum needed to form the shell is lost during the dealloying process) and a cross section of the final particles with the morphology determined from the particle size and composition. Comparing these particles to the TEM images, a number of points are worth noting. Particles of >3-4 nm are known to contain structure/porosity; especially for the particles starting rich in base metal. This porosity is exemplified in the large particle (>20 nm diameter) shown in Figure 1(o) of the d-$PtCo_3$/C catalyst, but looking at the distribution, this is at the upper end with minimum count and these few particles are not expected to contribute to the catalyst performance. The two other particles which are much more representative of the catalyst do not show significant porosity. An unfortunate side effect to the annealing process to alloy the Pt and Co and give the correct particle size is a broadening of the particle size distribution; especially at the high metal loadings used for commercial fuel cell catalysts, as used here. Tightening of this distribution would in effect increase the catalyst's activity and is currently a major focus in catalyst development.

Most initial testing of fuel cell catalysts occurs using the RDE technique, where only potentials above 0.8 V vs. RHE are accessible because of low oxygen mass transport, leading to a limiting current. The floating electrode technique provides results comparable to RDE results in this potential range. Figure 3(a) compares the CVs in nitrogen for the different Pt/C (i.e. x = 0) catalysts as a function of the different particle sizes at high potentials with the corresponding forward ORR scan (corrected for double layer charging - equivalent to those presented in ref [20]). The electrodes used for voltammetry under nitrogen have much higher loadings (roughness factors between 60 – 80) than for the ORR (roughness factors between 1 – 4) in order to more clearly demarcate the surface adsorption processes and render insignificant the capacitance contributions from the substrate (gold coated polycarbonate). Even though the roughness factors were ~20× greater, the y-axis scale is reduced by 400× showing the current associated with Pt oxide formation features is negligible compared to the ORR at potentials of 0.65 – 1.0 V vs. RHE.
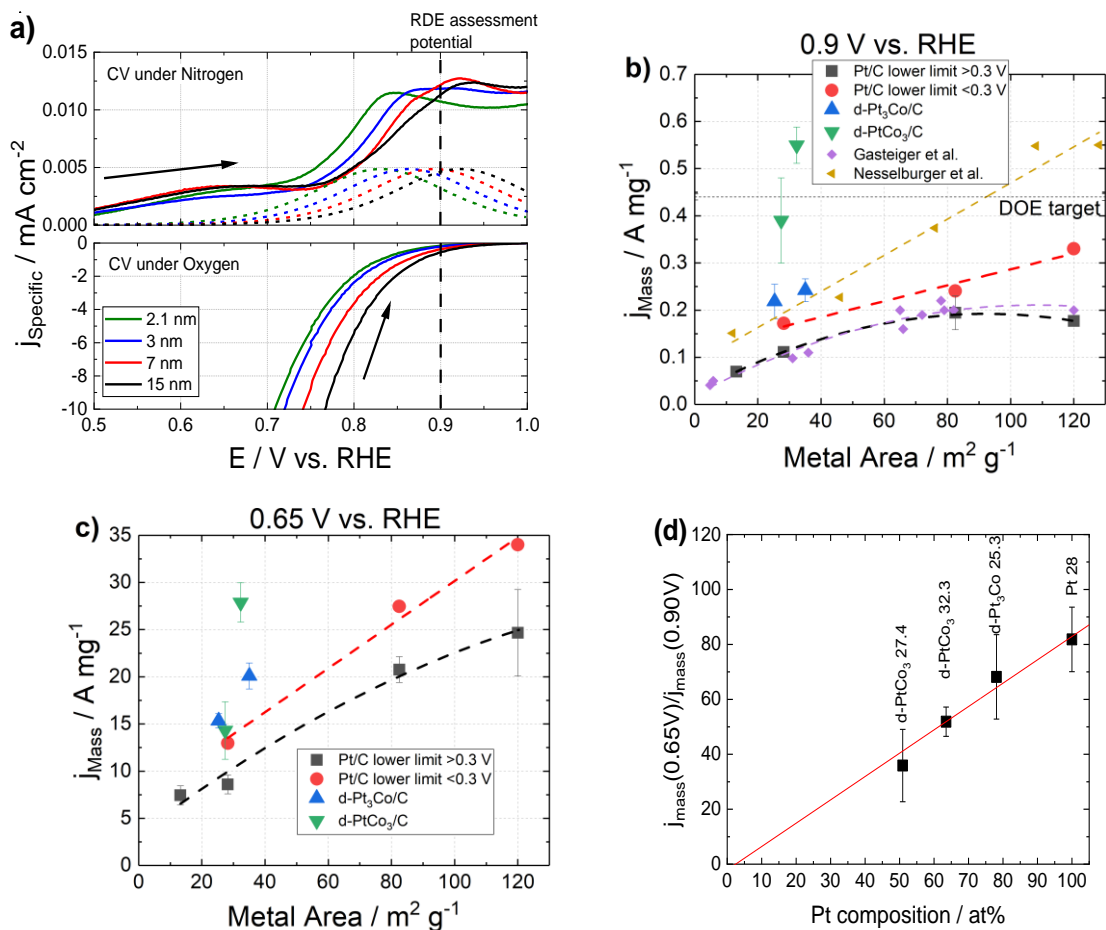
Figure 3. ORR mass activity comparison between catalysts of initial composition Pt$_{4-x}$Co$_x$ /C (x=0,1,3) as a function of potential and metal surface area| (a) CV of Pt/C catalysts of different particle sizes**.** CVs performed under nitrogen (top, note label scale reduced by 400×) and oxygen (bottom) for the anodic scan. ORR results have roughness factors between 1 - 4, CV measurements have roughness factors between 60 – 80. CV results under nitrogen also include the current due to the formation of blocking OH$_{ads}$ (dotted lines). Comparison of the mass activity at 0.9 V (b) and 0.65 V (c) of the catalysts listed in Table 1 as a function of their metal area. Points have been fitted with polynomial curves for guidance. Particle size effect literature comparison from Gasteiger *et al.* [32] and Nesselburger *et al.* [33]. (d) mass activity performance improvement associated with a 250 mV increase in overpotential (from 0.90 V to 0.65 V) for Pt/C and dealloyed catalysts with similar metal surface areas. Data for calculation from table in supporting information. 4 mol dm^{-3} HClO$_4$, 1 atm O$_2$, 298 K, 10 mV s^{-1}. Note: PtCo catalysts are listed with their nominal composition before dealloying in b) and c) while have their composition after dealloying in d).

For the CVs under nitrogen, as the particle size increases the onset of oxide formation is delayed to higher potentials. This delayed onset of oxide formation follows the ORR activity trend, showing oxide formation blocks the ORR, i.e. a $(1 - \theta)$ dependence, and has been outlined previously [34]. It is clear from this plot that the potential used for benchmarking ORR catalysts (0.9 V vs. RHE) is well within the region associated with oxide growth on the platinum surface. While an oxide coverage term has been recently included in activity models to simulate this blockage [35-38], these have mainly been fitted on one catalyst type (often a single crystal), and do not account for changes in the oxophilic nature of the Pt nanoparticle with particle size; this change can either be a change in site ratio (edges sites vs. facet sites) or a general increase in oxophilic nature of all atoms. The edge or low coordinated sites have been shown to have much stronger oxygen

binding energies, preferentially binding oxygen [39-40] and as smaller particles generally have a higher fraction of low coordinated or edge sites, they will be more oxophilic. Tritsaris *et al.* [41] showed that the energetics of a facet site adjacent to an edge tends towards that of an edge, causing the facets to become more oxophilic, however, this effect is only likely to be important for small particles. Yano *et al.* [42] showed that no electronic effects occur until the particle size is below 1 nm. Therefore, the change in site ratio factor is likely to dominate, as predicted previously [41, 43-46]. These low coordination sites are likely to be blocked by adsorbed oxides at high potentials and only activated at low potentials, if at all.

Figure 3(b) shows the mass activities at 0.9 V vs. RHE for the Pt/C and d-PtCo/C catalysts (see supporting information for table containing experimental results and errors). For the Pt/C catalysts (x = 0) there is a peak in the activity between $60 - 120$ m^2 g^{-1} ($2 - 4$ nm), as observed in the literature [32, 41, 43-49] (results from Gasteiger *et al.* [32] plotted for comparison). Within the errors of these measurements, this peak could also be interpreted as the mass activity levelling off, as observed by Sheng *et al.* [50] for particles below 5 nm. Note that our results do not involve cycling the potential below 0.3 V (before iR correction). This was to reduce the chance of hydrogen peroxide formation, which could be an issue at these high current densities [38, 48]. While the activity of the catalysts at 0.9 V agrees well with Gasteiger *et al.*'s results [32], they are low compared to recently reported results [51]. Nesselberger *et al.* [52] showed increasing the electrolyte concentration from 0.05 mol dm^{-3} to 0.4 mol dm^{-3} on polycrystalline Pt with the RDE gives a significant reduction in activity (from 1 to 0.4 mA cm^{-2}_{Spec}). This is in line with Omura *et al.* [53] who showed that perchloric acid is a specifically adsorbing anion. Measurements in this study were performed in 4 mol dm^{-3} $HClO_4$ which optimizes measurements at high current densities by reducing errors from *iR* correction. Moreover, anion concentration of 4 mol dm^{-3} is close to that which the catalyst may be exposed to within the ionomer environment of a fuel cell. Therefore, the slightly lower activity values at 0.9 V vs. RHE are undoubtedly due to the 40-fold increase in concentration of electrolyte to more realistic fuel cell values.

In terms of specific activity at 0.9 V the de-alloyed catalysts are clearly more active than the Pt/C catalysts with the activity order d-PtCo$_3$/C > d-Pt$_3$Co/C > all Pt/C catalysts (Figure 3(b)). Compared to the 6.9 nm Pt particles (roughly equivalent in size), the de-alloyed catalysts have increased specific activity between 1.5 - 2x for the d-Pt$_3$Co/C and 2.5 - 4x for the d-PtCo$_3$/C catalysts. Previously the increase in activity of Pt$_3$Co/C has been reported as 1.5 - 4x more active that Pt/C catalysts [53-56], with the activity ratio increasing as the alloying ratio reaches ~50% Co [54-55]. It is worth noting that while d-PtCo$_3$/C catalysts have the highest mass activities at 0.9 V vs. RHE, having non PGM metal compositions of ≥ 50 at. % leads to severe transition metal leaching which can affect the MEA performance [4]. As these experiments were performed in 4 mol dm^{-3} perchloric acid, the increased activity over Pt is expected to be slightly lower than literature comparisons in 0.1 mol dm^{-3} due to more pronounced anion adsorption on strained Pt alloy surfaces: Omura *et al.* [53] showed the 3x increase in activity of Pt$_3$Co/C in 0.5 mol dm^{-3} perchloric acid increases to 9x the activity of Pt in 0.01 mol dm^{-3} perchloric acid and this trend is likely to continue to 4 mol dm^{-3} perchloric acid. In terms of particle size effect, there is a weak correlation of **improved** performance for smaller particles (i.e. counter to the case with Pt) with the activity ordering **5.1 nm** >> **7.2 nm** > 4.6 nm ≈ 9.4 nm (bold associated with high Co content). This effect becomes more obvious at lower potentials (see below).

3.2 Particle size dependence of ORR at intermediate potentials (0.3-1.0 V)

Compared to the RDE approach, the floating electrode technique also allows assessment of ORR performance of catalysts in the range of potentials that the catalysts are exposed to in a fuel cell. Figure 4 shows the specific (a) and mass (b) activity of the ORR for the four pure Pt catalysts between 2 – 15 nm diameter. For each catalyst, three repeats were taken with the curve most representative of the average plotted. Using the floating electrode method, voltammetry can be measured across the complete operating range of a fuel cell in near mass transport free conditions, allowing activity values at high current densities to be measured rather than estimated. The DOE targets [1] of 0.44 A mg^{-1}_{Pt} at 0.9 V vs. RHE and 0.1 $g_{Pt,cathode}$ kW^{-1} (0.125 $g_{Pt,total}$ kW^{-1}) at 0.692 V vs. RHE are added to the mass activity graphs. These points assume no overpotential for the anode nor any hydrogen crossover and while these targets are at elevated temperature and pressure, they also include layer effects expected in a real MEA and therefore make a good initial comparison against the results presented here.
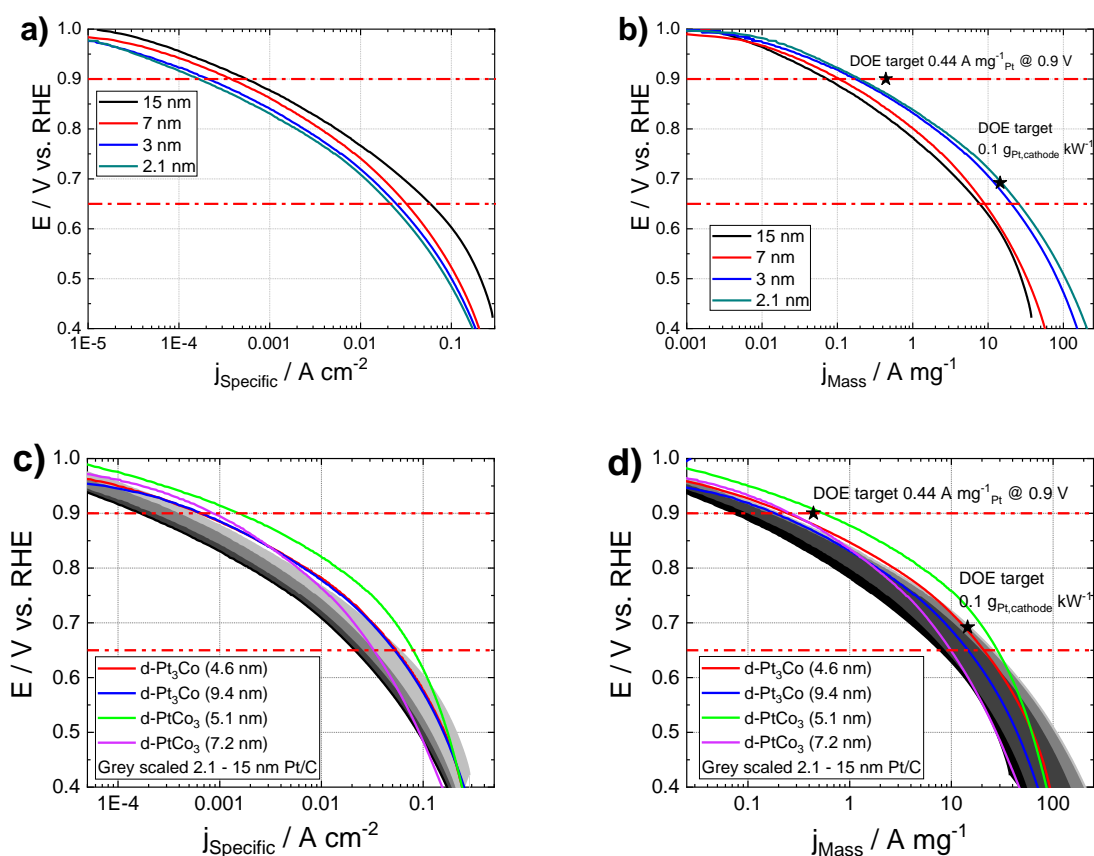
Figure 4. Particle size effect on ORR activity on catalysts with initial composition d-Pt$_{4-x}$Co$_x$ /C (x=0,1,3) over the potential range 0.4-0.95V | performance of Pt/C of different particles sizes with a roughness factor between 1 to 4 (2 − 25 μg_{Pt} cm^{-2}_{geo}) in specific activity (a) and mass activity (b). De-alloyed catalysts, d-Pt$_3$Co and d-PtCo$_3$ showing the specific (c) and mass (d) activities. 2.1 − 15 nm Pt/C catalysts from (a) and (b) shown in grey scale for comparison. Anodic scan, 4 mol dm^{-3} HClO$_4$, 1 atm H$_2$, 298 K, 10 mV s^{-1}, CE = Pt wire and RE = RHE. DOE targets of 0.44 A mg^{-1} at 0.9 V vs. RHE and 0.125 $g_{Pt,total}$ kW^{-1} (assumed to be 0.1 $g_{Pt,cathode}$ kW^{-1}) from [1] added to b) and d). The horizontal red lines represent the RDE reference potential (0.9 V) and a representative fuel cell operating point (0.65 V).

For Pt/C the specific activity decreases with reduced particle size across the whole measured potential range (0.4 - 1 V vs. RHE, iR corrected) in line with previous observations [32, 41, 43-49]. This has been attributed

to morphological changes in the particles' ratios of the crystal planes, with less active sites becoming dominant in smaller particles [41, 43-46]. The voltammograms for specific activity run nearly parallel across the whole measured potential range; the activity gain remains at high current densities for larger particles. However, looking at the mass activity, Figure 4(b), the ordering of the catalysts reverses with the smallest particle size having the highest performance in mass activity at all potentials. Furthermore, the difference between catalysts increases as the overpotential increases. The activities at 0.9 and 0.65 V vs. RHE are collected in Table s2 in the supporting information, and the mass activities as a function of metal surface area are presented in Figure 3(b) and (c).

Figure 4(c) and (d) shows the activity curves for a range of d-PtCo/C catalysts in comparison to the Pt/C catalysts of different particle size (grey scaled in the background) and the mass activities at 0.9 and 0.65 V vs. RHE of the catalysts are presented in Figure 3(b) and (c) in order to be comparable with previous results in the literature. These d-PtCo catalysts are compared at a range of particle sizes to make explicit the effect of particle size. This is especially important as state-of-the-art Pt catalysts are often slightly smaller (3 – 5 nm) than state-of-the-art de-alloyed catalysts (4 – 6 nm, with distributions towards the larger end) due to the annealing step needed to form the alloy and the requirement for formation of a Pt rich overlayer to stabilize the core (c.f. Figure 2). As described in the experimental section, all electrodes underwent an activation process involving cyclic voltammograms under a hydrogen and oxygen atmosphere with an upper limit of 1 V vs. RHE. The PtCo catalysts were de-alloyed before electrochemical testing to pre-form a Pt skin, as previously discussed. However, it is possible that the structure changes again during electrochemical testing. Repeated electrochemical cycling eventually gave reproducible performance which suggests the particles have reached a pseudo-steady state composition slightly different from their pre-tested state. It can be seen in Figure 4(c) that the specific activity of the two d-Pt_3Co/C catalysts of different particle sizes show very similar specific activities across the entire potential range studied with a response and curvature which is close to the Pt/C catalysts. In comparison, both d-$PtCo_3$/C catalysts show a response which is similar to each other (although offset in activity) but different to the other catalysts. Their response shows greater curvature with a tendency to "roll off" in performance at lower potentials compared to the Pt-rich and pure Pt catalysts. During multiple experiments, the specific activity of each catalyst had a narrow standard deviation between results (5 – 20%, with an average spread of 12%, see supporting information for repeats) except the 7.2 nm d-$PtCo_3$/C which increased to a 30% variation at 0.65 V vs. RHE. This could be due to its increased amorphous structure causing variations in the catalyst during testing or to Co leaching into the Nafion surrounding the catalyst particles, causing an increased proton resistance [57-58] or restriction of O_2 transport through the Nafion over layer expected here[59]. It is clear that increasing the Co content in the alloys makes producing catalysts with reproducible activity more challenging. In terms of particle size effects, it seems that there may be a tendency for higher specific activity of the smaller particles (i.e. the opposite trend compared to platinum), with the ordering of specific activity at 0.65 V being **5.1 nm** > 4.6 nm ≈ 9.4 nm > **7.2 nm** (**bold:** Co rich). It is interesting that the ordering **5.1 nm** > 4.6 nm ≥ 9.4 nm is the same as seen at 0.9 V, with the only change seen due to the 7.2 nm catalyst moving to 2nd from last position when the potential is changed from 0.65 to 0.9 V vs. RHE (see Table s2 in the supporting information).

Whilst all but the 7.2 nm de-alloyed catalysts show higher specific activities than all the Pt/C catalysts across the operating potential expected for a fuel cell (i.e. E > 0.6 V vs. RHE), this is not the case for mass activities. At low current densities, the de-alloyed catalysts are more active, but at high current densities, the smaller particle size Pt/C catalysts become equally or more active per gram of platinum (crossover at ~0.75 V vs RHE for the d-Pt$_3$Co/C and 0.65 V vs RHE for the d-PtCo$_3$/C under these conditions, Figure 4 (d)). The mass activities at 0.9 and 0.65 V vs. RHE are highlighted in Figure 3(b) and (c) and Figure 5(b) and (d). Comparing equivalent sizes, however, the de-alloyed catalysts remain more active with mass activities at 0.65 V vs. RHE of 1.7 – 2x for the d-Pt$_3$Co/C and 1.6 – 3x for the d-PtCo$_3$/C catalysts.

From 0.9 to 0.65 V vs. RHE, the mass activity increases by almost 2 orders of magnitude. At these high current densities, a peak in mass activity with decreasing particle size for the Pt/C catalysts is not observed, as exemplified by the mass activity comparison at 0.65 V vs. RHE shown in Figure 3(c), where the activity is still increasing at 2 nm in nearly linear fashion. For smaller catalyst particles which are highly dispersed across the carbon substrate, the diffusion of oxygen, protons and electrons is likely to be less constrained then when the Pt catalyst is spatially distributed in larger more active particles. In addition, with a large overpotential making reduction very favorable, having available sites becomes increasingly important. For example, at 1 A cm^{-2} for a 0.2 mg$_{Pt}$ cm^{-2} catalyst layer loading, an oxygen turnover (oxygen atoms reacted per exposed Pt atom) of ~5 molecules$_{O2}$ site^{-1} s^{-1} is needed when using the 2.1 nm particles. To sustain the same current density with 15 nm particles a turnover of ~45 molecules$_{O2}$ site^{-1} s^{-1} would be needed; over 9x the rate. This required higher turnover rate would increase the likelihood of a surface dependent limitation, e.g. surface blocking or a local diffusion limitation [12, 18-19, 60] or flooding from the product water. As these results show, catalysts of 3-5 nm provide optimum performance at 0.9 V vs. RHE but at higher current densities, smaller particles are still advantageous, pushing the optimum closer to 3 nm. This also applies to alloy catalysts, which due to their increased size (4.6 – 9.4 nm here) are found to be less active when compared to a smaller particle size Pt catalyst at high current densities and would therefore also benefit from a size reduction. Previously, this surface area dependence has been attributed to a local diffusion limitation caused by an ionomer layer over the catalysts [12, 60-61] calculated at ~12 s cm^{-1} over a number of structures. Unless the lattice parameter of the catalyst surface changes the packing density of the ionomer and therefore the oxygen diffusion rate, this should be the same for all the catalysts i.e. the specific activity should converge. This is not observed in Figure 4(a). An alternative explanation is that the difference in performance gain is associated with site blocking species [38], and the difference is a manifestation of the different electrocatalytic performance of the different catalysts.

Figure 5 pictorially represents the performance of all the catalysts depicted in Figure 4 at two potentials: 0.9 and 0.65 V. We also display an estimate of the instability region (associated with the size and bulk composition of Co@Pt$_{2ML}$ particles). This domain is demarcated by the line associated with the composition Co@Pt$_{2ML}$ – i.e. particles composed of a Co core coated by two monolayers of Pt. As described in section 3.1, all compositions to the left and below this composition will undergo further corrosion, so this line estimates the limiting composition line and any catalysts with bulk composition and size within the instability region are unlikely to survive electrochemical testing and will undergo severe corrosion. Figure 5(a) and (b) re-iterate the trends seen in Figure 3(b) and further suggests that the maximum specific and mass activities at 0.9 V are associated with particles close to the instability region, with a bulk Pt

composition of 60 at% and particle size of 4.1 nm. Because of the high cobalt content, such a particle would have to be composed of a core which was entirely (or almost entirely) composed of cobalt, which would be difficult to synthesize and prone to instability if the Pt shell was disrupted.
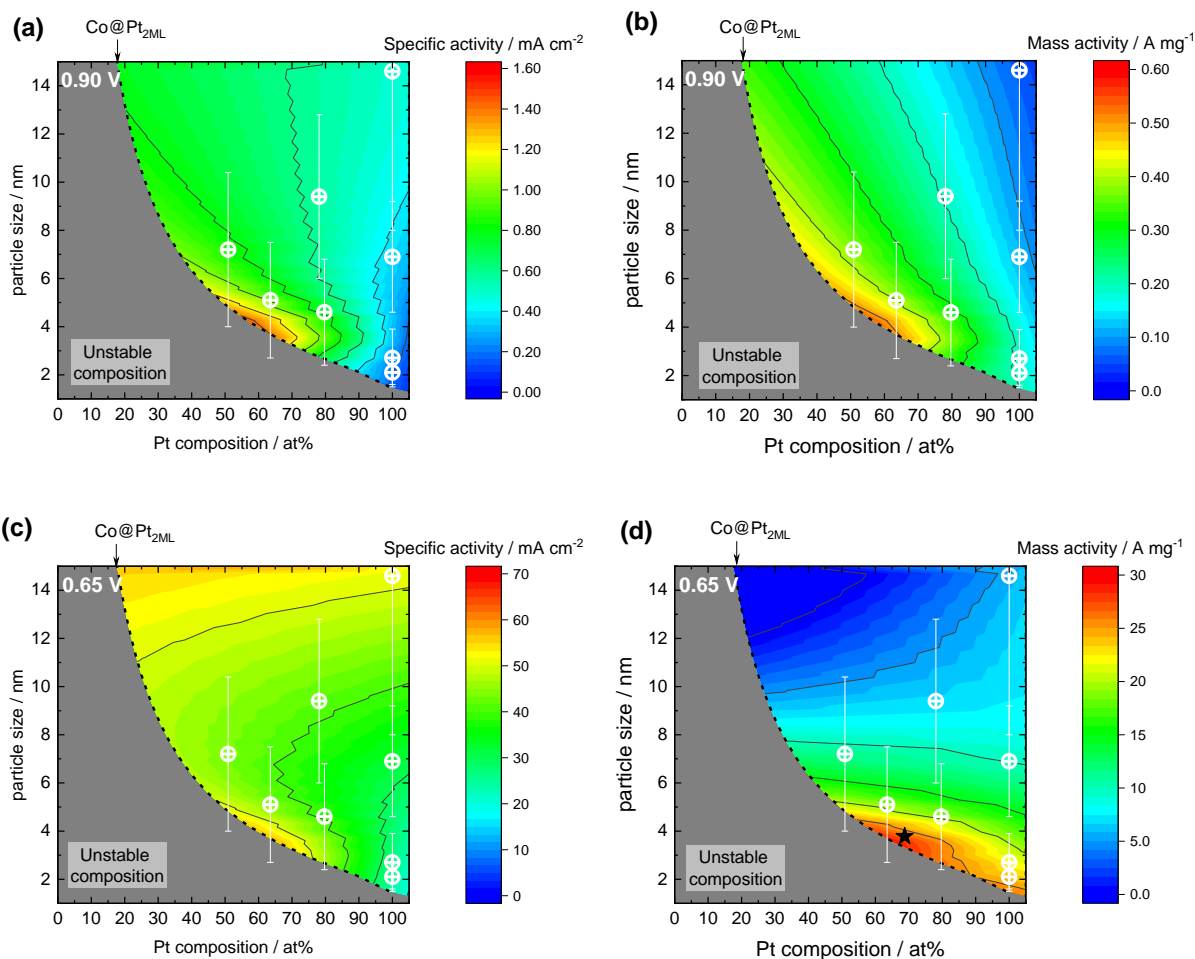
Figure 5. ORR specific and mass activity comparison between catalysts with initial composition d-Pt$_{4-x}$Co$_x$ /C (x=0,1,3) at 0.90V and 0.65V | Data taken from **Figure 4** and interpolated in order to produce the contour color map. Unstable composition bounded by Co@Pt$_{2ML}$ line which represents the limiting composition for a core shell catalyst particle with 2ML of Pt over a Co core. White points: catalyst compositions and sizes at which results were measured and used to generate performance plots. Black star: optimum composition 3.8 nm CoPt@Pt$_{1ML}$.

In both Figure 5(c) and (d) it can be seen that the most active catalysts are expected to have a bulk composition of between 60-70% Pt, and as small a particle size as possible – this is most clearly seen in Figure 5(d) in which the most active region for mass activity at 0.65 V is bounded by the two smallest Pt/C catalysts, and the smallest d-PtCo$_3$ and d-Pt$_3$Co catalysts. It is important to note that our conclusions are based on particles produced using a specific dealloying procedure, and that a different dealloying procedure may give rise to a slightly different result (as it may lead to a different particle morphology). In this region, it would appear that the zone offering the most active catalyst is around a bulk composition of 70 at% Pt. This composition would be satisfied by a 3.8 nm CoPt@Pt$_{1ML}$ particle (black star in Figure 5

(d)), which could be produced through dealloying a 4.1 nm CoPt particle and might provide about 30-40% higher mass activity than the most active of the catalysts we have tested. Note however that this prediction is an extrapolation from our data points and therefore could be prone to some error. If such a catalyst was to be produced, this would beg the question of how stable would it be? To achieve the EoL stability targets of >0.26 A mg_{Pt}^{-1} after 30 000 cycles[1] then the catalyst might benefit from a thicker Pt shell or a richer Pt composition, however this would be to the detriment to its activity.Figure 3(d) plots the ratio of mass activities at high current potential (0.65 V vs. RHE) to low current potential (0.9 V vs. RHE) vs. percentage Pt composition for catalysts with similar metal surface areas (25.3-32.3 m^2 g^{-1}). Matching the surface areas is important, as this should preclude issues associated with local mass transport effects. The Pt/C catalyst has about 80-fold the activity at 0.65 V vs. RHE compared to 0.9 V vs. RHE. For the d-PtCo3/C catalyst with 51% Pt and 49% Co, this activity gain is only about 35-fold, showing a greater loss in the improvement of mass activity (from low current potentials to high current potentials) when there is more Co in the structure. This reiterates the issue about faster "roll-off" in catalyst activity seen for the Co-rich catalysts discussed previously, and evident in Figure 4(c). This gives the site blocking mechanism some credence, as we see a linear dependence of the gain with cobalt content for catalysts with very similar surface areas – i.e. an electronic effect which is dictated by the amount of cobalt. Hence, it is important to understand the affinity of these surfaces for adsorbed species. Ideally, we would have liked to relate this performance gain to variations in lattice parameters to give an indication of the surface strain, however, these were not possible to measure due to the low crystallinity of the two d-PtCo$_3$/C catalysts. More studies on the precise nature of this interface and how it affects the activity at high overpotentials could be highly beneficial for the production of optimized ORR catalysts.

3.3   Modelling ORR performance and the effect of site blocking

In order to differentiate between the electrokinetic performance of the different catalysts, we have used our previously developed electrokinetic model to assess the degree of site blocking for the ORR which occurs at both high potentials (due to oxide growth) and low potentials (due to oxygen reduction intermediates and H$_{upd}$) [38]. The blocking of the surface reduces the number of sites available for oxygen adsorption, which at lower potentials becomes the rate limiting step. In this approach we have previously only considered one type of site as active in the catalyst, associated with the facets of the particles, but as will be shown below the edges become active for the ORR at very low potentials.

As we are far away from the equilibrium potential, we utilize a Tafel type expression to take into account the overpotential effect associated with driving the ORR[62]. The overall current is directly dependent upon the number of free sites available for oxygen adsorption, θ_{free}, and is presumed to be limited by a slow step associated with a single electron transfer associated with a molecular symmetry factor, β,

$$j = -j_0 \left(\frac{c}{c_0}\right)^\gamma \theta_{free} e^{\left(\frac{-\beta F\left(E - E'_{O_2,H^+}\right)}{RT}\right)}$$

(1)

where j is the kinetic current density, j_0 is the exchange current density, F is Faradays constant, E is the potential applied, E'_{O_2,H^+} is the reversible potential for the ORR under the conditions of the experiment (1 atm O$_2$, 4 mol dm^{-3} HClO$_4$) , R is the ideal gas constant, T is the temperature, c and c_o are the oxygen

concentration at the catalyst surface and the reference oxygen concentration, γ the reaction order for oxygen (presumed to be one). The number of free surface sites is dictated by the coverage of different species on the surface which are adsorbed more strongly than O_2 and which thus block available sites for the initial adsorption step. It is also assumed that oxygen adsorption (at least in the rate determining step) requires a single adsorption site.

Surface coverage, θ, of adsorbed species is assumed to follow the relationship described in Equations 2 and 3.

$$Pt + H^+ + e^- \rightleftharpoons PtH_{ad}$$
$$Pt + H^+ + O_2 + e^- \rightleftharpoons PtOOH_{ad} \qquad \theta_{H_{ad},OOH_{ad}} = \frac{1}{1 + exp\left[\frac{(E - E'_{H_{ad},OOH_{ad}})q_H F}{RT}\right]} \qquad (2)$$

$$Pt + H_2O \rightleftharpoons PtOH_{ad} + H^+ + e^-$$
$$PtOH_{ad} \rightleftharpoons PtO + H^+ + e^- \qquad \theta_{OH_{ad},O_{ad}} = \frac{1}{1 + exp\left[\frac{-(E - E'_{OH_{ad},O_{ad}})q_O F}{RT}\right]} \qquad (3)$$

Where $\theta_{H_{ad},OOH_{ad}}$ represents the coverage of blocking species at low potential due to ORR intermediates such as HOO$_{ad}$ and also H$_{ad}$ [38], and $\theta_{OH_{ad},O_{ad}}$ represents the coverage of blocking species at high potential due to oxide species. q is similar to the Temkin interaction parameter. The isotherms generated for $\theta_{H_{ad},OOH_{ad}}$, and $\theta_{OH_{ad},O_{ad}}$ are equivalent to Langmuir isotherms when $q=1$ and are symmetrically stretched out when q<1 (see SI for more details). $E'_{H_{ad},OOH_{ad}}$ and $E'_{OH_{ad},O_{ad}}$ represent the equilibrium potential for the adsorption processes, i.e. the potential at which the associated coverage is ½. θ_{free} is then calculated from $\theta_{H_{ad},OOH_{ad}}$, and $\theta_{OH_{ad},O_{ad}}$ under the assumption that the adsorbed species do not interact, but that one of the species adsorbs more strongly than the other such that they both fulfil the energetic requirements of their respective isotherms

$$\theta_{free} = (1 - \theta_{H_{ad},OOH_{ad}})(1 - \theta_{OH_{ad},O_{ad}}) \qquad (4)$$

The Tafel slope $\left(\frac{\partial \eta}{\partial log_{10}|i|}\right)$, is sometimes used as a parameter to provide some mechanistic information on the reaction. For our electrokinetic interpretation given above, we can estimate the value of the Tafel slopes under different conditions. When the surface is free of any blocking species (i.e. no H$_{ad}$, OOH$_{ad}$, OH$_{ad}$, O$_{ad}$), then θ_{free}=1, and the Tafel slope is

$$\left(\frac{\partial \eta}{\partial log_{10}|j|}\right)_{adsorbate-free} = -\frac{RT log_e(10)}{\beta F} \qquad (5)$$

However, as we will see below, it seems that the catalyst surface is rarely, if ever, totally free of adsorbates, so it is difficult to see this Tafel slope. At high potentials, where $\theta_{H_{ad},OOH_{ad}} \cong 0$, the surface is blocked only by OH$_{ad}$ and O$_{ad}$, and the Tafel slope has the form (derivation in the supporting information)

$$\left(\frac{\partial \eta}{\partial log_{10}|j|}\right)_{oxide} = -\frac{RT log_e(10)}{(\beta+q_O)F} \qquad (6)$$

The ORR results were fitted for the four d-PtCo/C and four Pt/C catalysts. Further details of the fitting procedure are provided in the supporting information, and the fitting results for all the catalysts are provided in Table 2 (see supporting information for further plots comparing the Pt/C catalysts and also how the fit parameters change with catalyst composition).

The specific activity curves, and the associated fits (dotted red lines) are shown in Figure 6 (a) for the four catalysts with similar surface area (curves for all catalysts are in the supporting information), as we would expect similar mass transport effects (if they exist) for all four. It can be seen that in all cases the fits match well to the ORR currents. Indeed, as seen from the inset in Figure 6 (a), the fits provide a good representation of the current over more than three orders of magnitude of current range. Note that the fits do not require any sort of mass transport limitation to limit the performance at high overpotential. Also shown in the inset of that figure are the average Tafel slopes derived from the fitting results for adsorbate free and oxide covered surfaces (calculated using Eq 5 and 6 and shown for each catalyst in Table 2).

Table 2. Performance parameters of the catalysts d-Pt$_{4-x}$Co$_x$ /C (x=0,1,3) determined from fitting of electrochemical results | Fitting parameters and parameters derived from the fitting parameters for the four d-PtCo/C and four Pt/C listed in order of increasing Co content and particle size. j$_{kin}$ represents the kinetic current in the absence of any blocking species on the surface, and j$_{oxide}$ represents the region where the surface is covered with OH$_{ad}$ and O$_{ad}$. Fitting curves shown in Figure 6. Details of fitting procedure in the supporting information.

Catalyst		Fitted Parameters						Derived parameters				
								θ_{free}			Tafel slope / mV decade^{-1}	
	Size /nm	$E'_{H_{ad},OOH_{ad}}$ /V	q_H	$E'_{OH_{ad},O_{ad}}{}^a$ /V	$q_O{}^b$	β ^{c}	j$_{o,spec}$ /µA cm^{-2}	0.9 V	0.65 V	j$_{calc}$ @ 0.9 V / mA cm^{-2}	j$_{adsorbate-free}$	j$_{oxide}$
Pt/C	2.1	0.637	0.295	0.830	0.5	0.431	2.48	0.195	0.523	0.121	137	64
Pt/C	3	0.620	0.312	0.862	0.5	0.431	2.57	0.314	0.580	0.202	137	64
Pt/C	7	0.630	0.323	0.892	0.5	0.431	3.43	0.447	0.559	0.386	137	64
Pt/C	15	0.589	0.384	0.922	0.5	0.431	4.88	0.601	0.710	0.736	137	64
d-Pt$_3$Co	4.6	0.601	0.267	0.825	0.5	0.332	49.7	0.182	0.605	0.641	178	71
d-Pt$_3$Co	9.4	0.620	0.270	0.832	0.5	0.350	35.2	0.200	0.562	0.620	169	70
d-PtCo$_3$	5.1	0.717	0.303	0.846	0.5	0.380	50.1	0.231	0.306	1.51	155	67
d-PtCo$_3$	7.2	0.721	0.278	0.890	0.5	0.402	12.2	0.397	0.313	0.832	147	66
Average		0.642	0.304	0.862	0.5	0.399	20.1	0.321	0.520	0.631	150	66

^{a} for Pt/C, the values of the potentials are constrained to be the offset by the same amount as the shift in oxide peaks
^{b} for all catalysts q$_o$ is constrained to be ½
^{c} for Pt/C, results are fit with the same value of β i.e. one fit parameter is optimized across four catalysts.

At high potential, the Tafel slope well-matches the change in current density, but it is clear that there is no obvious region displaying a slope associated with the unblocked surface, and instead there is a continuous change in slope. The calculated exchange current density increases with particle size for the Pt/C utilizing a common value of β which is fit to give the best fit across all four Pt/C catalysts. These Pt/C exchange current densities are similar to values we have previously measured [38], and somewhat lower than the values seen in fuel cells [37]. An increase in exchange current density for the fuel cell results would be expected because of the higher operating temperature (80°C vs. 25°C in these experiments). See supporting information Table s4 for comparison to other catalysts measured in the literature. In contrast,

the exchange current densities on the d-PtCo/C catalysts are about an order of magnitude larger, with the largest values obtained for the 5.1 nm d-PtCo$_3$, which is the most active catalysts. The higher exchange current density on these catalysts matches what is experimentally determined. The molecular symmetry factor, β, is higher for the Pt/C catalysts (NB, this parameter was a common fit parameter across all Pt/C catalysts), although all the materials show a value between 0.33 and 0.43. These values indicate a highly asymmetrical process which contributes to a large Tafel slope in the absence of adsorbates.

Figure 6(b) gives the derived coverage of OH$_{ad}$ and O$_{ad}$ on the catalyst surfaces as a function of potential (dotted lines represent extrapolation beyond the experimental data). It can be seen that compared to the Pt/C catalyst, all the cobalt containing catalysts show a negative shift in the potential for oxide growth of ca. 40 mV (Table 2) for particles of similar size, apart from the 7.2nm d-PtCo$_3$ which shows a similar value to the 7nm Pt/C. Displayed in Table 2 are the calculated number of free adsorption sites at 0.9 and 0.65 V. At 0.90 V, used as the test potential for RDE characterization, there are slightly fewer free sites on the d-PtCo/C catalysts compared to the Pt/C catalyst, although the number of free sites on the Pt/C catalysts does increase with particle size, as might be expected from the voltammetry in Figure 3(a). The value of q_O was fixed at 0.5, as it was found that when this parameter was allowed to vary, it fell in the range 0.4 - 0.5 for all catalysts (see supporting information).
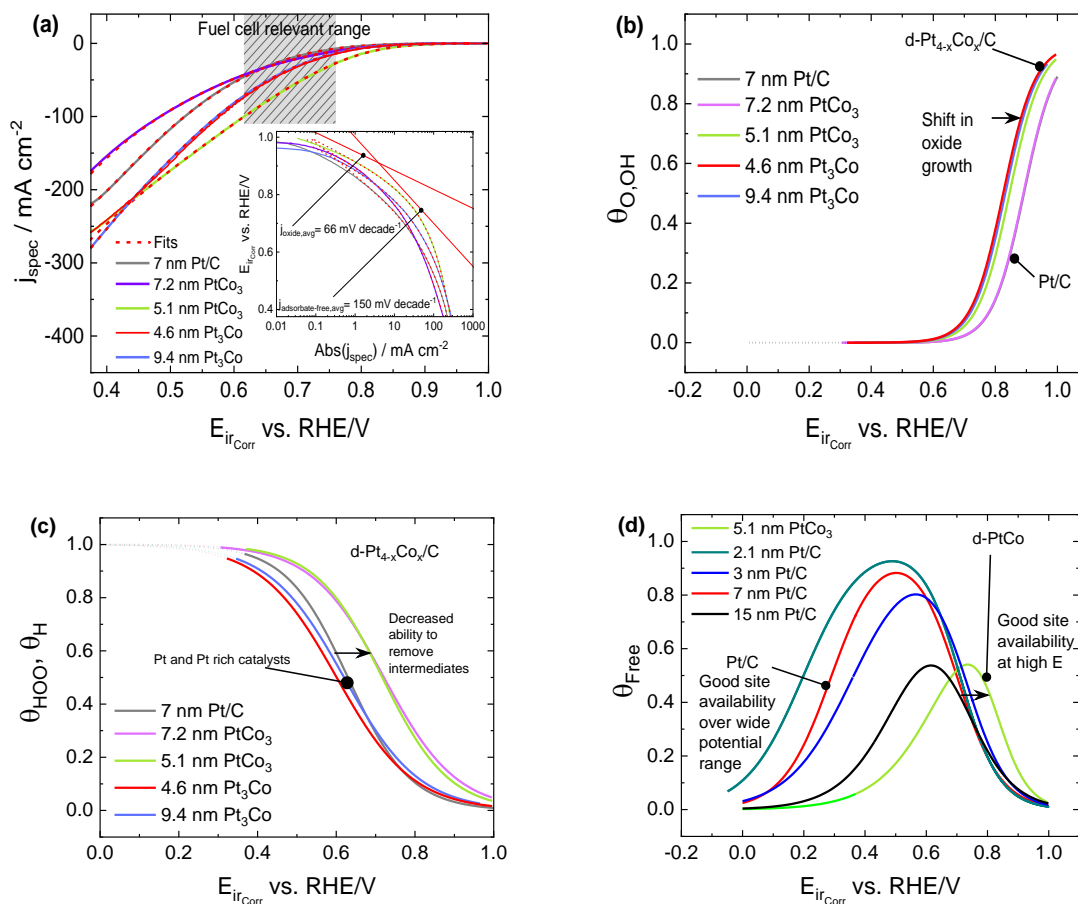
Figure 6. ORR electrokinetic fitting and derived species coverages for catalysts with initial composition Pt$_{4-x}$Co$_x$/C (x=0,1,3) with similar surface areas | (a) Specific activity data and model fit (dashed red line) to equation (1). Inset: data plotted on logarithmic scale. (b) Derived coverage of O and OH on the catalyst surfaces from the model fitting parameters and Eq 3; (c) Derived coverage

In contrast, Figure 6(c) provides the coverage of oxygen containing blocking species (or H_{ads}) on the surface, both of which block oxygen adsorption at low potential. In this case, we find that $E'_{H_{ad},OOH_{ad}}$ is highly dependent on the catalyst composition. The Pt/C catalysts and the high platinum content d-Pt₃Co/C catalysts show similar results, whereas the d-PtCo₃/C catalysts show a positive shift by about 100 mV, but this has a negative, rather than positive effect on performance. It is presumed that the blocking of the surface is associated with an oxygen reduction intermediate. As we saw previously [38], it is intriguing that the 1/2-wave potential for the adsorption ($E'_{H_{ad},OOH_{ad}}$) on the d-PtCo/C catalysts (0.589-0.721 V – see Table 2) is close to the equilibrium potential for oxygen reduction to peroxide

$$O_2+2H^++2e^-\rightleftharpoons H_2O_2 \qquad E^0=0.695V \qquad (7)$$

In our previous paper we suggested that the blocking species was either a strongly bound peroxide intermediate or a strongly bound superoxide intermediate, OOH_{ad}. The presence of these species on the surface would not necessarily lead to excessive amounts of hydrogen peroxide generation if they were strongly bound. Within the H_{upd} region however, a pathway for desorption of these species becomes possible leading to formation of H_2O_2

$$OOH_{ad}+H_{ad}\rightleftharpoons H_2O_2 \qquad (8)$$

It is clear from Figure 6(c) that the surface of both the d-PtCo/C and Pt/C catalysts become significantly blocked at low potentials. This point is highlighted by Figure 6(d) which provides the free coverage available for oxygen adsorption, θ_{free}, on the catalyst as a function of potential (calculated according to Eq (4)). Although the d-PtCo/C catalysts provide a larger number of free sites at high potential, their surface becomes increasingly congested at lower potential, leading to a deficit of oxygen adsorption sites. At 0.65 V, we find that the Pt/C and high Pt content d-Pt₃Co/C catalysts have >20% more free sites than the average site availability on the d-PtCo₃/C catalysts (Table 2). From these results we can understand the reason for the Pt/C catalyst overtaking the d-PtCo/C catalysts in the low potential region – it is due to the significant amounts of site blocking which occur on the d-PtCo/C surfaces, especially the high Co content catalysts at low potentials. We can also use these results to understand the significant increase in performance for Pt/C that we see in transitioning from 0.9 V to 0.65 V, and why we don't see the same performance gain in d-PtCo/C catalysts as shown in Figure 3(d). The reason is twofold – although the d-PtCo/C catalysts have a higher exchange current density, they also have a lower value of β (and thus higher Tafel slope). At the same time, the number of free sites available for oxygen adsorption at 0.65 V is less than for Pt/C.

What do these results mean in terms of catalyst design and testing? There are three major lessons to be learnt:

a) 0.9 V is not necessarily a good reference potential to judge performance at lower potentials –the effect of strength of adsorption and coverage of intermediates also needs to be considered over the range of operating potentials.

b) In terms of the d-PtCo/C catalysts, it would appear that even though the surface is relatively free of oxide at high potentials, a significant amount of the surface is blocked within the window at which fuel cells operate (0.6-0.75 V). Being able to decrease the coverage of those species might lead to a further two-fold improvement in performance at high overpotentials due to a larger number of available sites.

c) Computational studies which ignore the effect of bystander species (anions, H_{upd}, oxygen reduction intermediates) may not be able to accurately predict the performance of catalyst under a realistic operating regime.

3.4 Particle size dependence of the ORR at potentials <0.3 V and activation of the ORR at low potentials

In section 3.3 the lower potential limit was set to 0.3 V in order to limit the production of hydrogen peroxide. Below 0.3 V vs. RHE, the activity changes drastically and instead of a continuous increase in current, two peaks are seen for the three Pt/C particle sizes, 2.1, 3 and 7 nm, Figure 7(a). Once the potential is swept to still lower values, there is a dramatic reduction in the current before reaching a minimum current at ca. 0 V vs. RHE after which the hydrogen evolution reaction (HER) dominates.

It is surprising that two peaks are seen in the H_{upd} region. These two peaks are very similar to those recently observed for the HOR (Red curve in the inset of Figure 7) using the floating electrode technique [14, 63] and are only visible at very low loadings where polarization resistances through the catalyst layers don't broaden the features. The catalyst loadings used in these results are between $0.5 - 2$ µg cm^{-2}$_{Pt}$ ($R_f = 0.6 - 0.8$). These low loadings were used to maintain resolution of the two peaks, and to reduce layer polarization and bulk mass transport effects. The 15 nm catalyst is not shown due to complications in the measurement, possibly due to polarization effects through the layer due to the large quantity of carbon needed to achieve sufficient catalyst surface area (~9× more for the 14.6 nm than the 2.1 nm particle size catalyst to achieve the same Pt surface area).

On the basis of the similarity to the HOR results [20], we assign the peaks to the ORR activity of facets (peak at ca. 0.24 V, $E_{Peak,high}$), and edges (peak at ca. 0.1 V, $E_{Peak,low}$). As discussed above, the low coordination sites are likely to be blocked by adsorbed oxides or anions at high potentials [41, 43-46] and only activated at low potentials, if at all. As seen for the HOR, Figure 7(a) shows that the 2 nm Pt/C catalyst has two peaks of approximately equal size, and as the Pt particle size increases, $E_{Peak,high}$ (i.e. the peak associated with facet sites) increases in size relative to $E_{Peak,low}$ (edge sites). The change in ratio of edges to facets follows what would be expected for a truncated octahedron geometry [20]. In addition, the potential gap between the two peaks of the ORR at about 0.13 V ($0.1 - 0.23$ V vs. RHE) is close to that observed for the HOR (~0.2 – 0.38 V vs. RHE), red curve in the inset in Figure 7, and to the peak difference between the oxide stripping peaks, Figure 2(b) (~0.6 – 0.75), further confirming these phenomena are linked. Assuming Tafel kinetics with a gradient of 59 mV dec^{-1} (25 °C and α = 1) [32], Equation 9, a peak separation of 120 mV would show an activity difference of ~120× between the two sites. Previous predictions of the HOR/HER suggest a 60

– 80 fold difference in activity of the edges to facets in the presence of anions or 130-140 fold when anion free [20].

$$log(-I) = log(I_0) - \frac{\alpha F}{2.3RT}\eta \tag{9}$$

The magnitude of the ORR current decreases at potentials less than $E_{Peak,low}$ and $E_{Peak,high}$ because the respective sites become covered by H_{upd}, blocking the absorption of oxygen. Hence at 0.02 V, a minimum is seen as the Pt surface is substantially blocked towards the ORR, with the current being less than half of the peak current (suggesting that the reduction in current cannot solely be explained by a switch of mechanism from 4e$^-$ to 2e$^-$ oxygen reduction). Within this low potential region, some current is due to the HER reaction (which will occur positive of 0 V vs. RHE, as the hydrogen gas concentration << 1 atm), some due to direct reaction of oxygen with H_{upd} to produce hydrogen peroxide or protonated superoxide (followed by subsequent electrochemical regeneration of the H_{upd}), and some due to electrochemical oxygen reduction to hydrogen peroxide and water. To exemplify the distributions of current as the potential tends towards zero, CVs under nitrogen (showing HER in the absence of HOR) and oxygen for the 2.1 nm Pt/C catalyst are compared in the inset in Figure 7(a). Also plotted is the difference between these two curves - labelled 'CV(O$_2$) – CV(N$_2$)'. At 0 V the CV under nitrogen crosses the current axis at ca. 110 mA cm$^{-2}_{Spec}$, 30% of the current density of the ORR at ca. 350 mA cm$^{-2}_{Spec}$. Figure s12 in the supporting information shows the HER and ORR distribution for each catalyst showing the same trends. This seems to support the explanation that the catalyst remains active to HER (i.e. has a high coverage of H_{upd}), but is substantially deactivated to the ORR, as H_{upd} blocks O$_2$ adsorption.
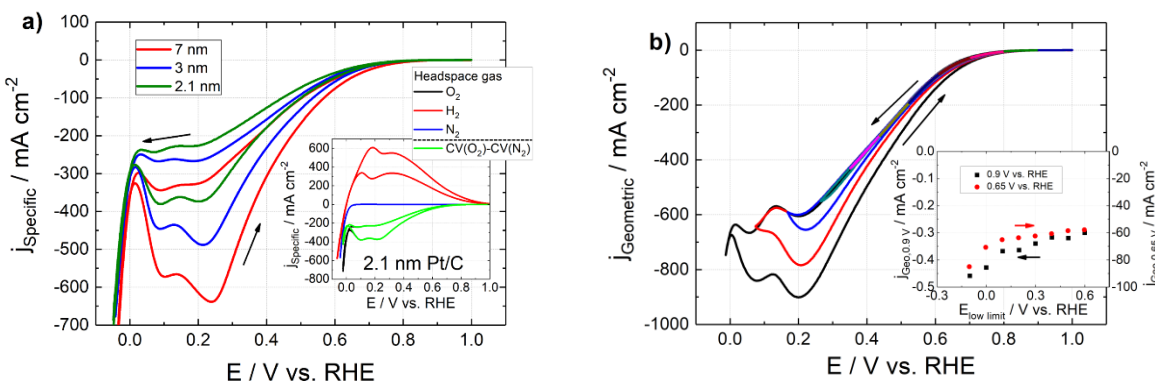
Figure 7. Effect on ORR of scanning to low potential | a) ORR of Pt/C catalysts at 2.1, 3 and 7 nm particle size, scanning between -0.02 – 1 V vs. RHE. Inset shows the ORR and HOR activity of the 2.1 nm particle size catalyst, HOR from ref [20], completed under the same conditions as the ORR. b) Window opening of the ORR using the 3 nm Pt/C catalyst. The CVs were run in 4 mol dm^{-3} HClO$_4$ at 10 mV s^{-1} at 298 K under 1 atm. CE = Pt wire, RE = RHE.

Below 0 V vs. RHE, the voltammograms exponentially increase in current density as would be expected for the HER. As there is little hydrogen in the vicinity of the catalyst particles (it diffuses away quickly due to the high mass transport achieved at these electrodes), the curve will be dominated by the HER, which when measured in a nitrogen atmosphere yields currents between 100 and 140 mA cm$^{-2}_{Spec}$ (see supporting information, Figure s12).

An interesting aspect of scanning to potentials below 0.3 V vs. RHE is an activation of the ORR which had not previously been observed to this extent [14, 38]. The activation of the catalyst to the ORR upon scanning to low potentials is most clearly seen in Figure 7(b), in which "window opening" voltammetry is performed. If the potential does not go below 0.3 V vs. RHE, the voltammetry closely re-traces itself, showing almost the same current on the forward and reverse scans. Once the lower scan limit is below 0.2 V vs. RHE, there is an activation of the ORR leading to significant hysteresis, with the reverse scan (i.e. increasing the applied potential) occurring at significantly higher currents than the preceding negative going scan. In all cases the subsequent negative going scan retraces the previous path, showing that the activation is short lived and deactivates during the period of the scan. As the lower potential limit is further decreased, the amount of ORR activation further increases, showing the largest amount of activation for the most negative scan (-0.02 V vs. RHE). Supporting Table s2 shows the specific activity values for the reverse scan at 0.9 and 0.65 V vs. RHE for the three catalysts when scanned from a lower potential of -0.01 V vs. RHE, which on average are 43% greater than when the potential does not go below 0.3 V vs. RHE. While the extent of this increase in performance at lower potentials could not be observed in the RDE, scanning to lower potentials has been shown to increase the activity at 0.9 V vs. RHE [33, 64].

The commonly observed hysteresis between the forward and reverse scan seen during RDE results has been discussed previously as the adsorption of oxide species (O, OH, OOH) [32] for which, due to the dynamic nature of the measurement, different surface coverages of site blocking species are expected when scanning from low potentials to high potentials. However, the fact that the potential must be set below 0.3 V vs. RHE in order to remove the blocking species argues for either a very strongly adsorbed oxide, or some other process such as anion adsorption. In addition, scanning to -0.01 V vs. RHE increases the mass activity at both 0.90 V and 0.65 V. In Figure 3(a) and (b) we also plot the performance of the catalysts with a lower scan limit of -0.01 V vs. RHE. The mass activity at 0.9 V vs. RHE increases in a linear fashion with surface area, showing no peak mass activity. Both results are double layer and *iR* corrected (corrections for the data scanned to a lower limit of 0.3 V vs. RHE are shown in Figure s6, supporting information), with no large change in the shape seen due to the corrections. ORR activities at 0.9 V vs. RHE obtained on RDE results from Nesselburger *et al.* [33] are plotted in Figure 3(a) which also show a linear activity improvement. This activity improvement could be due to further reduction of oxide sites, or desorption of anions blocking ORR sites increasing the number of sites active for the ORR. In an operating fuel cell, the likelihood of the cathode going below 0.3 V vs. RHE is low, unless specific design steps were taken, for instance short-circuiting the stack under fuel starvation. Therefore, particle design should focus on the peak mass activity observed when the potential scan range is >0.3 V vs. RHE giving the optimum particle size between 3 – 5 nm. Alternatively, it would be beneficial to design catalysts or catalyst supports which prevent these edge sites from becoming deactivated e.g. by preventing catalyst particles from direct contact with ionomer whilst keeping them close enough to have sufficient ionic conduction, as has been suggested previously [65].

4   Conclusion

In this paper, a range of well-characterized industrially relevant catalysts has been studied to assess the alloying effect of cobalt and the effect of particle size on the ORR.

The composition of the catalysts has been well characterized and a calculation procedure for assessing dealloying in PtCo/C catalysts developed. This has been used to develop understanding of the likely stability range of those catalysts associated with the dealloying process. Co rich particles are expected to be less stable than Pt rich particles. We have used these calculations to estimate the likely geometry of particles on the basis of their bulk composition and particle size. We see that the d-Pt_3Co/C and d-$PtCo_3$/C compositions were most likely to have a one and two monolayer Pt skin, respectively, where a monolayer thickness represents the size of an FCC unit cell. A stability diagram allows us to estimate the range of compositions and particle sizes that can be produced through the dealloying process.

The performance of the resulting $Pt_{4-x}Co_x$ /C (x=0,1,3) catalysts has been assessed as a function of potential using the floating electrode technique. The **specific activity** of the Co-containing catalysts compared to the pure Pt/C catalysts is greater by a fixed factor throughout the whole working potential range of a fuel cell. The smaller Pt/C catalysts show increased **mass activity** at E <0.75 V vs RHE compared to the d-Pt_3Co/C and E <0.65 V vs RHE compared to the d-$PtCo_3$/C. However, the dealloyed PtCo catalysts show better mass activity at all potentials when compared to Pt/C catalysts of the same size. We estimate that at 0.65 V a catalyst composed of 3.8 nm $CoPt@Pt_{1ML}$ particles may offer a 30-40% greater mass activity than any of those we have tested here.

For the catalysts studied, and especially for a subset chosen to have the same specific surface area, we find that specific activity does not tend towards a set value at high current densities as a surface independent diffusion limitation (e.g. Nafion overlayer) would suggest but remains linear giving some credence to a site blocking mechanism being the limitation at high specific current densities.

Between 0.9 and 0.65 V vs. RHE, the increase in current density for the Pt/C catalyst is close to 80×, however this activity gain decreases linearly with increasing Co alloying with d-$PtCo_3$ being only 35x more active as the potential changes. Through modelling the electrochemical response, we find that the exchange current densities are about 10-fold greater in the d-PtCo/C catalysts, but this is coupled to a decrease in β, and thus they show an increase in the effective Tafel slope. In contrast, at 0.65 V, the Pt/C catalyst has ~20% **more** potential oxygen adsorption sites. Both of these factors contribute to the greater increase in activity for the Pt/C catalysts as the potential is changed from 0.9 V to 0.65 V. We have developed an electrochemical model based on site blocking at both high and low potentials which adequately represents the performance of the catalysts with potential and can accurately fit the data over more than three orders of magnitude of current.

Depending on the lower potential limit, the mass activity at 0.9 V vs. RHE either increased continuously with decreasing particle size (<0.3 V vs. RHE) or reached a peak at $3 - 5$ nm (>0.3 V vs. RHE), both trends previously observed in the literature. The former perhaps shows activation of more oxophilic sites such as low coordination edges sites; the latter however, is more relevant to commercialization since a cathode layer in a fuel cell should not often see very low potentials. A large hysteresis was observed at low potentials indicative of site blocking species; these blocking species are a) only removed at very low potentials suggesting either a very strongly adsorbed oxide, or some other process such as anion adsorption and b) play a large role in the observed limiting current density. The effect of surface species

in the intermediate and low potential region warrants further investigation to optimize catalysts for high current density performance.

Finally, at low potentials within the H_{upd} region, two peaks were observed with similar properties to those observed for the HOR, suggesting the phenomenon is linked in the two reactions; hypothesized here as two sites, edges being $E_{Peak,low}$ and facets being $E_{Peak,high}$. Again, these peaks were observable due to the low layer resistances within the floating electrode technique, allowing definition in the CVs not otherwise possible to observe.

We see that the extrapolation of the performance of catalysts based on their activity at 0.9 V is fraught with a number of confounding issues which can easily lead to an incorrect ranking of catalysts. Specifically, it seems that site blocking is an important aspect which has not been adequately explored or included in computational models exploring the activity of catalysts.

Suggestions for future work would involve extending the electrochemical model we have provided to include individual contributions from the edges and facets discussed above and to better understand the mechanism behind the activation processes obvious at low potentials. It is also interesting to see that the geometrical modelling of the dealloying process suggests that the most favored de-alloyed morphologies may change with initial particle size. This area should be examined in greater details and the dealloying diagram "tuned" by calibrating it to a larger dataset of particle size and composition (and alloying compounds).

5   Supporting Information

Supporting information is provided including comparison or catalyst size and composition, floating electrode results as a function of catalyst and scan potential, literature comparison of our results to state of the art catalysts, analysis of the XRD pattern of $PtCo_3$; compositional line scans of Pt_3Co/C and $PtCo_3/C$ catalysts; discussion of iR and double layer correction to the data; example of repeat runs in independent electrodes; analysis of activity as a function of Co content; ORR versus HER contribution to current close to 0V RHE; description of the approach used to estimate the composition and morphology of particles following dealloying displayed in Figure 2 in the paper; description of the electrochemical isotherm sued to approximated the coverage of species on the surface; derivation of equation 6 in the main paper; all of the fitting results for the eight catalysts tested used in producing Table 2; and a description of the fitting procedure used to fit the data. The data used in the preparation of the figures in this paper is available for download[66].

7 References

1.   Fuel Cell Technologies Office Multi-Year Research, Development, and Demonstration Plan Section 3.4 Fuel Cells, Office of Energy Efficiency and Renewable Energy, https://www.energy.gov/sites/prod/files/2017/05/f34/fcto_myrdd_fuel_cells.pdf.

2.   Martens, S.; Asen, L.; Ercolano, G.; Dionigi, F.; Zalitis, C.; Hawkins, A.; Martinez Bonastre, A.; Seidl, L.; Knoll, A. C.; Sharman, J.; Strasser, P.; Jones, D.; Schneider, O., *Journal of Power Sources* **2018,** 392, 274-284.

3.   Cui, C.; Gan, L.; Heggen, M.; Rudi, S.; Strasser, P., *Nat Mater* **2013,** 12 (8), 765-771.

4.   Han, B.; Carlton, C. E.; Kongkanand, A.; Kukreja, R. S.; Theobald, B. R.; Gan, L.; O'Malley, R.; Strasser, P.; Wagner, F. T.; Shao-Horn, Y., *Energy & Environmental Science* **2015,** 8 (1), 258-266.

5.   Chen, C.; Kang, Y.; Huo, Z.; Zhu, Z.; Huang, W.; Xin, H. L.; Snyder, J. D.; Li, D.; Herron, J. A.; Mavrikakis, M.; Chi, M.; More, K. L.; Li, Y.; Markovic, N. M.; Somorjai, G. A.; Yang, P.; Stamenkovic, V. R., *Science* **2014,** 343 (6177), 1339-1343.

6.   Stamenkovic, V.; Markovic, N. *2015 DOE Hydrogen and Fuel Cells Program Review: Nanosegregated Cathode Catalysts with Ultra-Low Platinum Loading*; U.S. Department of Energy, 2015, 2015.

7.   Huang, X.; Zhao, Z.; Cao, L.; Chen, Y.; Zhu, E.; Lin, Z.; Li, M.; Yan, A.; Zettl, A.; Wang, Y. M.; Duan, X.; Mueller, T.; Huang, Y., *Science* **2015,** 348 (6240), 1230-1234.

8.   Bu, L.; Zhang, N.; Guo, S.; Zhang, X.; Li, J.; Yao, J.; Wu, T.; Lu, G.; Ma, J.-Y.; Su, D.; Huang, X., *Science* **2016,** 354 (6318), 1410-1414.

9.   Li, M.; Zhao, Z.; Cheng, T.; Fortunelli, A.; Chen, C.-Y.; Yu, R.; Zhang, Q.; Gu, L.; Merinov, B. V.; Lin, Z.; Zhu, E.; Yu, T.; Jia, Q.; Guo, J.; Zhang, L.; Goddard, W. A.; Huang, Y.; Duan, X., *Science* **2016,** 354 (6318), 1414-1419.

10.   Yoshida, T.; Kojima, K., *The Electrochemical Society Interface* **2015,** 24 (2), 45-49.

11.   Stephens, I. E. L.; Rossmeisl, J.; Chorkendorff, I., *Science* **2016,** 354 (6318), 1378-1379.

12.   Kongkanand, A.; Mathias, M. F., *The Journal of Physical Chemistry Letters* **2016,** 7 (7), 1127-1137.

13.   Kucernak, A. R.; Toyoda, E., *Electrochemistry Communications* **2008,** 10 (11), 1728-1731.

14.   Zalitis, C. M.; Kramer, D.; Kucernak, A. R., *Physical Chemistry Chemical Physics* **2013,** 15 (12), 4329-4340.

15.   Pinaud, B. A.; Bonakdarpour, A.; Daniel, L.; Sharman, J.; Wilkinson, D. P., *Journal of The Electrochemical Society* **2017,** 164 (4), F321-F327.

16.   Inaba, M.; Jensen, A. W.; Sievers, G. W.; Escudero-Escribano, M.; Zana, A.; Arenz, M., *Energy & Environmental Science* **2018,** 11 (4), 988-994.

17.   Inaba, M.; Jensen, A. W.; Sievers, G. W.; Escudero-Escribano, M.; Zana, A.; Arenz, M., *Energy & Environmental Science* **2018**.

18.   Greszler, T. A.; Caulk, D.; Sinha, P., *Journal of The Electrochemical Society* **2012,** 159 (12), F831-F840.

19.   Owejan, J. P.; Owejan, J. E.; Gu, W., *Journal of The Electrochemical Society* **2013,** 160 (8), F824-F833.

20.   Zalitis, C. M.; Kucernak, A. R.; Sharman, J.; Wright, E., *Journal of Materials Chemistry A* **2017,** 5 (44), 23328-23338.

21.   Wakisaka, M.; Hyuga, Y.; Abe, K.; Uchida, H.; Watanabe, M., *Electrochemistry Communications* **2011,** 13 (4), 317-320.

22.   van der Vliet, D. F.; Wang, C.; Li, D.; Paulikas, A. P.; Greeley, J.; Rankin, R. B.; Strmcnik, D.; Tripkovic, D.; Markovic, N. M.; Stamenkovic, V. R., *Angewandte Chemie International Edition* **2012,** 51 (13), 3139-3142.

23.   Rudi, S.; Cui, C.; Gan, L.; Strasser, P., *Electrocatalysis* **2014,** 5 (4), 408-418.

24.   00-029-0498, *Natl. Bur. Stand. (U. S.) Monogr.* **1978,** 25 (15), 168.
25.   00-029-0499, *Natl. Bur. Stand. (U. S.) Monogr.* **1978,** 25 (15), 170.
26.   Teo, B. K.; Sloane, N. J. A., *Inorganic Chemistry* **1985,** 24 (26), 4545-4558.
27.   Van Hardeveld, R.; Hartog, F., *Surface Science* **1969,** 15 (2), 189-230.
28.   Lopez-Haro, M.; Dubau, L.; Guetaz, L.; Bayle-Guillemaud, P.; Chatenet, M.; Andre, J.; Caque, N.; Rossinot, E.; Maillard, F., *Appl. Catal. B-Environ.* **2014,** 152, 300-308.
29.   Gan, L.; Heggen, M.; Rudi, S.; Strasser, P., *Nano Letters* **2012,** 12 (10), 5423-5430.
30.   Wang, C.; Chi, M.; Wang, G.; van der Vliet, D.; Li, D.; More, K.; Wang, H.-H.; Schlueter, J. A.; Markovic, N. M.; Stamenkovic, V. R., *Advanced Functional Materials* **2011,** 21 (1), 147-152.
31.   Lorenz, C. D.; May, R.; Ziff, R. M., *Journal of Statistical Physics* **2000,** 98 (3), 961-970.
32.   Gasteiger, H. A.; Kocha, S. S.; Sompalli, B.; Wagner, F. T., *Applied Catalysis B: Environmental* **2005,** 56 (1-2), 9-35.
33.   Nesselberger, M.; Ashton, S.; Meier, J. C.; Katsounaros, I.; Mayrhofer, K. J. J.; Arenz, M., *Journal of the American Chemical Society* **2011,** 133 (43), 17428-17433.
34.   Marković, N. M.; Ross, P. N., *Surface Science Reports* **2002,** 45 (4), 117-229.
35.   Wang, J. X.; Zhang, J.; Adzic, R. R., *The Journal of Physical Chemistry A* **2007,** 111 (49), 12702-12710.
36.   Jinnouchi, R.; Kodama, K.; Hatanaka, T.; Morimoto, Y., *Physical Chemistry Chemical Physics* **2011,** 13 (47), 21070-21083.
37.   Subramanian, N. P.; Greszler, T.; Zhang, J.; Gu, W.; Makharia, R. R., *ECS Transactions* **2011,** 41 (1), 985-1007.
38.   Markiewicz, M.; Zalitis, C.; Kucernak, A., *Electrochimica Acta* **2015,** 179, 126-136.
39.   Wei, G.-F.; Liu, Z.-P., *Physical Chemistry Chemical Physics* **2013,** 15 (42), 18555-18561.
40.   Jinnouchi, R.; Suzuki, K. K. T.; Morimoto, Y., *Catalysis Today* **2016,** 262 (Supplement C), 100-109.
41.   Tritsaris, G. A.; Greeley, J.; Rossmeisl, J.; Nørskov, J. K., *Catal Lett* **2011,** 141 (7), 909-913.
42.   Yano, H.; Inukai, J.; Uchida, H.; Watanabe, M.; Babu, P. K.; Kobayashi, T.; Chung, J. H.; Oldfield, E.; Wieckowski, A., *Physical Chemistry Chemical Physics* **2006,** 8 (42), 4932-4939.
43.   Peuckert, M.; Yoneda, T.; Betta, R. A. D.; Boudart, M., *Journal of The Electrochemical Society* **1986,** 133 (5), 944-947.
44.   Kinoshita, K., *Journal of The Electrochemical Society* **1990,** 137 (3), 845-848.
45.   Shao, M.; Peles, A.; Shoemaker, K., *Nano Letters* **2011,** 11 (9), 3714-3719.
46.   Perez-Alonso, F. J.; McCarthy, D. N.; Nierhoff, A.; Hernandez-Fernandez, P.; Strebel, C.; Stephens, I. E. L.; Nielsen, J. H.; Chorkendorff, I., *Angewandte Chemie International Edition* **2012,** 51 (19), 4641-4643.
47.   Takasu, Y.; Ohashi, N.; Zhang, X. G.; Murakami, Y.; Minagawa, H.; Sato, S.; Yahikozawa, K., *Electrochimica Acta* **1996,** 41 (16), 2595-2600.
48.   Chen, S.; Kucernak, A., *The Journal of Physical Chemistry B* **2004,** 108 (10), 3262-3276.
49.   Mayrhofer, K. J. J.; Blizanac, B. B.; Arenz, M.; Stamenkovic, V. R.; Ross, P. N.; Markovic, N. M., *The Journal of Physical Chemistry B* **2005,** 109 (30), 14433-14440.
50.   Sheng, W.; Chen, S.; Vescovo, E.; Shao-Horn, Y., *Journal of The Electrochemical Society* **2012,** 159 (2), B96-B103.
51.   Shinozaki, K.; Morimoto, Y.; Pivovar, B. S.; Kocha, S. S., *Electrochimica Acta* **2016,** 213, 783-790.
52.   Nesselberger, M.; Roefzaad, M.; Fayçal Hamou, R.; Ulrich Biedermann, P.; Schweinberger, F. F.; Kunz, S.; Schloegl, K.; Wiberg, G. K. H.; Ashton, S.; Heiz, U.; Mayrhofer, K. J. J.; Arenz, M., *Nat Mater* **2013,** 12 (10), 919-924.
53.   Omura, J.; Yano, H.; Tryk, D. A.; Watanabe, M.; Uchida, H., *Langmuir* **2014,** 30 (1), 432-439.
54.   Toda, T.; Igarashi, H.; Uchida, H.; Watanabe, M., *Journal of The Electrochemical Society* **1999,** 146 (10), 3750-3756.

55.   Paulus, U. A.; Wokaun, A.; Scherer, G. G.; Schmidt, T. J.; Stamenkovic, V.; Radmilovic, V.; Markovic, N. M.; Ross, P. N., *The Journal of Physical Chemistry B* **2002,** 106 (16), 4181-4191.

56.   Wakabayashi, N.; Takeichi, M.; Uchida, H.; Watanabe, M., *The Journal of Physical Chemistry B* **2005,** 109 (12), 5836-5841.

57.   Cai, Y.; Kongkanand, A.; Gu, W.; Moylan, T. E., *ECS Transactions* **2015,** 69 (17), 1047-1061.

58.   Ahluwalia, R. K.; Wang, X.; Peng, J.-K.; Kariuki, N. N.; Myers, D. J.; Rasouli, S.; Ferreira, P. J.; Yang, Z.; Martinez-Bonastre, A.; Fongalland, D.; Sharman, J., *Journal of The Electrochemical Society* **2018,** 165 (6), F3316-F3327.

59.   Durst, J.; Chatenet, M.; Maillard, F., *Physical Chemistry Chemical Physics* **2012,** 14 (37), 13000-13009.

60.   Ono, Y.; Ohma, A.; Shinohara, K.; Fushinobu, K., *Journal of The Electrochemical Society* **2013,** 160 (8), F779-F787.

61.   Liu, H.; Epting, W. K.; Litster, S., *Langmuir* **2015,** 31 (36), 9853-9858.

62.   Antoine, O.; Bultel, Y.; Durand, R., *Journal of Electroanalytical Chemistry* **2001,** 499 (1), 85-94.

63.   Zalitis, C. M.; Sharman, J.; Wright, E.; Kucernak, A. R., *Electrochimica Acta* **2015,** 176, 763-776.

64.   Shinozaki, K.; Zack, J. W.; Richards, R. M.; Pivovar, B. S.; Kocha, S. S., *Journal of The Electrochemical Society* **2015,** 162 (10), F1144-F1158.

65.   Yarlagadda, V.; Carpenter, M. K.; Moylan, T. E.; Kukreja, R. S.; Koestner, R.; Gu, W.; Thompson, L.; Kongkanand, A., *ACS Energy Letters* **2018,** 3 (3), 618-621.

66.   Zalitis, C.; Kucernak, A.; Sharman, J., Data used in the preparation of the figures in the paper ""Electrochemical measurement of intrinsic oxygen reduction reaction activity at high current densities as a function of particle size for Pt4-xCx /C (x=0,1,3) catalysts", DOI: <<Inserted during proof stage>>. 2020.